Quaternary Science Reviews 298 (2022) 107800

Contents lists available at ScienceDirect

Quaternary Science Reviews

journal homepage: www.elsevier.com/locate/quascirev

An ensemble of Antarctic deglacial simulations constrained by geological observations

Mark L Pittard, Pippa L Whitehouse, Michael J Bentley*, David Small

Department of Geography, Durham University, Durham, DH1 3LE, United Kingdom

A R T I C L E I N F O

Article history:
Received 30 October 2021
Received in revised form
16 September 2022
Accepted 24 September 2022
Available online 9 November 2022

Handling Editor: Dr Giovanni Zanchetta

A B S T R A C T

The Antarctic ice sheet has the potential to make a significant contribution to future sea-level rise. Understanding this potential and making projections of future ice sheet mass change requires use of numerical models. Confidence in model projections can be improved by hindcasting: testing the model against past ice sheet changes. Robust deglacial model reconstructions are also used to correct satellite gravimetric measurements of current change for glacial isostatic adjustment processes. Here we present a new model ensemble of post-Last Glacial Maximum Antarctic deglaciation reconstructions. The ensemble is generated using the Parallel Ice Sheet Model (PISM) in which we vary a range of parameters including key glaciological controls, basal sediment strength, mantle viscosity, and climate forcing. We test the ensemble results against a database of geological constraints, and develop a new scoring scheme that allows us to determine metrics of model performance against past ice sheet grounding line extent, ice sheet thickness, and thinning rates, as well as present-day ice sheet configuration. We discuss the parameter combinations that lead to the highest-scoring simulations and we also compare our ensemble performance with existing published deglacial models, using the same scoring scheme. Exploring the characteristics of the highest-scoring ensemble members highlights some key features of deglacial behaviour including a relatively narrow range of past excess ice volumes at the LGM, Holocene retreat behind present-day grounding lines with commensurate volume minima, and readvance behaviours. The comparison also allows us to identify areas where more geological data would have high constraining power for ice sheet models.

1. Introduction

Understanding Antarctica's contribution to future sea-level change is of great societal importance as it has the potential to make a large contribution to rising sea level in the coming decades to centuries (DeConto and Pollard, 2016). Model projections of the Antarctic contribution show significant differences, with some of these associated with mechanisms of ice sheet change (Edwards et al., 2019). One way to help resolve these differences is to compare ice sheet model output with past ice sheet changes; successful hindcasting can improve confidence in future projections as it suggests the model is accurately representing the key processes driving ice sheet retreat.

Antarctica's current contribution to sea-level change can be estimated through three satellite-based approaches: altimetry, gravimetry and the input-output method (Shepherd et al., 2012). Each of these approaches has strengths and weaknesses but both the altimetry and gravimetry approaches require some knowledge of ice sheet history in order to make corrections for ongoing change in the underlying bedrock elevation. The movement of the crust is caused by changes in ice loading and, depending on the mantle viscosity, this can impose vertical motion for decades to millennia. Models of glacial isostatic adjustment (GIA) provide Antarctic-wide estimates of solid Earth deformation (Ivins and James, 2005; Whitehouse et al., 2012b; Argus et al., 2014). Reducing the uncertainty in GIA model estimates of the magnitude and spatial pattern of deformation depends on improving our knowledge of Earth structure and past ice sheet change (Sasgen et al., 2017; Whitehouse et al., 2019). Therefore, our ability to quantify current sea-level contributions as well as accurately predict future change depends on a knowledge of past ice sheet change and requires approaches to compare geological observations to ice sheet model

* Corresponding author.
E-mail address: m.j.bentley@durham.ac.uk (M.J. Bentley).

https://doi.org/10.1016/j.quascirev.2022.107800

output.

Antarctica has relatively few areas of ice-free terrain onshore, and there are significant challenges to working on the continental shelf. For this reason there are limited geological observations of past ice sheet change across the continent and the available data are not evenly spread in space or time (Bentley et al., 2014). Models of the deglacial history of Antarctica therefore often rely either on geological reconstructions derived from sparse spatial information, or on numerical simulations of ice sheet change that are constrained using the geological measurements and so allow glaciologically consistent interpolation between areas where constraints exist. A deglacial model describes changes in ice extent and volume, typically for the interval between the Last Glacial Maximum (LGM) and the present day (PD) which is the interval where most geological data exists (Bentley et al., 2014).

During the LGM global mean sea level was approximately 120–135 m lower than present (Clark and Mix, 2002; Bintanja and van de Wal, 2008; Lambeck et al., 2014) with the majority of the displaced water located in ice sheets in the Northern Hemisphere. The volume of the Antarctic ice sheet at the LGM has been estimated by three different approaches; far-field sea-level budget calculations, deglacial histories reconstructed from paleo-observations, and ice sheet modelling (Bentley, 1999, 2010). Recent decades have seen a wide range of estimates of Antarctic contribution to LGM sea-level fall, (see Simms et al. (2019) for a review) but it has been argued that the most recent estimates are converging towards 9.9 ± 1.7 m of sea-level equivalent (SLE) volume (Simms et al., 2019). Despite early budget calculations requiring an Antarctic LGM volume of > 10 m SLE (Simms et al., 2019), recent global ice sheet reconstructions (Gowan et al., 2021) have been able to close the global sea-level budget at the LGM with an Antarctic contribution < 10 m.

In addition to differences in the total contribution of the Antarctic Ice Sheet to sea-level change since the LGM, the distribution, timing, and rate of post-LGM Antarctic ice mass change also varies between deglacial models. Current reconstructions of the LGM ice sheet vary between an ice sheet with a laterally extensive grounding line, but which is relatively thin (Golledge et al., 2012; Whitehouse et al., 2012a; Ivins et al., 2013; Gomez et al., 2013; Briggs et al., 2014), and a thick ice sheet with a less advanced grounding line (Peltier, 2004; Argus et al., 2014; Lambeck et al., 2014). The timing and rate of subsequent mass loss also varies between deglacial histories. Some published deglacial models include pulses of rapid deglaciation (Argus et al., 2014; Golledge et al., 2014) whilst others show a more steady and gradual deglaciation (Whitehouse et al., 2012b; Ivins et al., 2013).

To evaluate the simulations from deglacial models a range of methods based on paleo-observations have been developed (Briggs et al., 2014; DeConto and Pollard, 2016; Ely et al., 2019). These evaluation methods are designed to either exclude poorly performing model simulations (using filters or 'sieves') or directly assess and compare the accuracy of the simulations (using scores). A sieve is a pass/fail filter which is used to exclude simulations that display unrealistic behaviour based on a set of criteria. Another benefit of sieves is that they enable a manageable number of (realistic) ensemble members to be used in further analysis, as it can be impractical to individually analyse hundreds to thousands of simulations. This is important given increasing computational power and the production of large ensembles of simulations (Briggs et al., 2014; DeConto and Pollard, 2016; Maris et al., 2014; Albrecht et al., 2020b) in which climate or glaciological parameters are varied. One common sieve used is the volume of the ice sheet, often expressed as SLE volume, at various points in time. Far-field records of sea-level change extend further into the past than near-field records of ice sheet extent variation, enabling us to estimate long-term Antarctic contributions to sea-level change. For example, a study by DeConto and Pollard (2016) excluded simulations which did not show a change in sea level during the Pliocene of 10–20 m and during the last interglacial of 3.6–7.4 m SLE. This example also highlights a risk of the use of a priori knowledge in the sieve method as the range of 3.6–7.4 m SLE has subsequently been disputed (Edwards et al., 2019), which would change the interpretation of the results. Alternatively, a scoring method can be used to numerically compare the relative performance of different ensemble simulations to see which best match our knowledge of the evolution of Antarctica, by comparing model results directly against observations. This approach provides a useful metric for evaluating large ensembles (Briggs et al., 2014; DeConto and Pollard, 2016). In this paper, we present a suite of simulated deglacial histories of Antarctica that are consistent with observations of past change and present a new scoring method for assessing deglacial models. Our methodology is described in three steps. We first detail the Parallel Ice Sheet Model (PISM) which we use to generate an ensemble of Antarctic deglacial simulations, employing a range of climate, mantle viscosity and glaciological parameters. Secondly, we introduce a sieving and scoring methodology that uses geological and glaciological constraints to assess the accuracy of each simulated deglacial history in the ensemble. The method incorporates paleo-observations of ice extent, ice thickness, and thinning rates into a scoring framework. It also includes an assessment of how well the simulations reproduce present-day glaciological observations. Thirdly, we run two model ensembles. The first investigates the role of climate forcing and mantle viscosity using a relatively coarse set of glaciological parameters. Using our scoring method we analyse the initial ensemble results to select an optimum climate and mantle viscosity for a second ensemble where we carry out a more detailed investigation of the glaciological parameter space. We identify the highest scoring model simulations from both ensembles and compare the scores and characteristics of previously published deglacial models with our 10 best-scoring simulations. Finally, we discuss the implications of our results for our understanding of the past deglacial behaviour of the Antarctic ice sheet.

2. Ice sheet model methods

We use the Parallel Ice Sheet Model (PISM) version 1.1 (Bueler et al., 2007; Winkelmann et al., 2011; Aschwanden et al., 2012; Reese et al., 2018) with modified surface mass balance lapse rates (Albrecht and other PISM authors, 2019) and variations to the slipperiness at the grounding line detailed herein.

PISM has previously been used to model the Antarctic Ice Sheet over a glacial cycle (Albrecht et al., 2020a, 2020b) using an ensemble method. Our modelling approach is different to Albrecht et al. (2020a, 2020b) in four main ways. First, we take a different approach to the PISM parameterisation that sets the basal till in the grid cell landward of the grounding line to be 100% saturated. This is a parameterisation which has become increasingly important over the evolution of PISM [e.g., Golledge et al., 2015], particularly when simulating a glacial cycle. In our preliminary investigations this parameterisation prevented the ice sheet from advancing to the continental shelf, but if it was turned off the ice sheet would advance and never retreat. To address this we created the Slipperiness of the Grounding Line (SGL) parameterisation (see section 2.1), which varies the saturation level in the till (between 0 and 100%), and tested it within our ensemble. Albrecht et al. (2020a) used an alternative parameterisation in which, instead of the landward grid cell being saturated, every newly grounded grid cell is immediately saturated as the ice sheet advances. A second modelling difference relates to the value of the pseudo-plastic exponent, a parameter which controls the rate of basal sliding within PISM. Albrecht et al. (2020a, 2020b) varied the pseudo-plastic exponent within their ensemble: we select a fixed value (0.75) but note that the value used matches the one used in the best-fit simulation of Albrecht et al. (2020b) and subsequently the initMIP-Antarctica model intercomparison (Seroussi et al., 2019). Thirdly, we explore a different and larger parameter space (4 parameters, 256 models) than Albrecht et al. (2020b) by running a broad initial ensemble (6 parameters, 192 models) followed by a more detailed ensemble that uses optimal parameters selected from the first ensemble (3 parameters, 440 models). Fourthly, to ensure manageable computation demands, we use a slightly coarser horizontal resolution (20 km vs 16 km) than Albrecht et al. (2020a).

In this section we briefly describe the physics underlying PISM, the model parameters that can be varied, and our approach to climate forcing. Details of the parameters used in our two model ensembles are given in sections 4 and 5.

2.1. PISM physics

PISM calculates ice flow using a hybrid shallow ice approximation (SIA) and shallow shelf approximation (SSA) scheme. The SIA dominates ice flow where there is grounded ice, while the SSA dominates where there is floating ice. The hybrid nature relates to the treatment of ice streams, where both the SIA and SSA are important to the overall ice flow. PISM additionally includes an enthalpy-based 3-D thermodynamic scheme that has the capacity to simulate ice at the pressure melting point, both subglacially (basal melt) and englacially (temperate ice).

The hybridised ice flow is calculated by combining the SIA and SSA calculations and adopting a pseudo-plastic sliding law. The SSA component of the solution yields only small basal velocities across much of the ice sheet and hence basal sliding is predominantly controlled by consideration of whether the driving stress exceeds the yield stress of a deformable till; where the driving stress is higher, significant basal sliding may occur. The yield stress is determined by the Mohr-Coulomb criterion (Cuffey and Paterson, 2010) which depends on the effective pressure in the till layer as well as the till friction angle.

Effective pressure is primarily controlled by the water content of the till layer. We assume a 2 m-thick till layer across Antarctica (PISM default value), with local basal melt causing the till to saturate with water. The till friction angle is determined through a piecewise linear relationship in which the till angle is defined to be smaller (weaker till) at lower bed elevations and greater (stronger till) at higher bed elevations.

An optional PISM parameterisation, *-tauc_slippery_grounding_lines*, specifies that the till layer in any grid point below sea level that lies adjacent to the grounding line will be saturated. We introduce a new parameter, Slipperiness of Grounding Line (SGL), that we use in conjunction with the standard *-tauc_slippery_grounding_lines* option, and which allows us to vary the percentage saturation (0–100%) of grid cells immediately upstream of the grounding line. The standard option applies 100% saturation; for our experiments this means that the till depth and water depth are both 2 m (the default value in PISM). However, if we set the SGL parameter to be, for example, 50%, all grid cells immediately upstream of the grounding line are assumed to have a water depth of 1 m in a 2 m till layer.

Finally, the calving of ice shelves is an important physical process which is poorly understood, particularly in the context of a glacial cycle where only scarce proxy data are available to determine past calving behaviour. We simultaneously use two parameterisations to control the rate of calving. The first makes use of a regionally varying thickness calving value (see Supplementary Data), which in each time step automatically calves ice that is thinner than a defined thickness from the ice shelf front. The second applies the eigen calving law (Levermann et al., 2012), which compares the product of the principal components of the horizontal strain rates to an eigen calving value in order to calculate an average calving rate. In effect, it compares the rate of stretching within the ice shelf with a set value to determine if, based on its flow rate and thickness, the ice is stable. If it is not, the ice will be calved.

2.2. Model initialisation and boundary conditions

For each simulation a smoothing run of 1000 years (SIA physics only) is followed by a thermal spin-up period of 200,000 years (constant present day climate). A dynamic interglacial spin-up period is then simulated using a constant present-day climate for 30,000 years, with the climate forcing scenarios (section 2.4) running from thereon. The glacial cycle length depends on the ice core used to drive the climate forcing scenario. We run the model for 1000 years beyond the present day to fully capture the variability in ice sheet dynamics during the present interglacial.

The model domain uses the Durham University bedrock map (DUbmap, see Supplementary Data), which is based on Bedmap2 (Fretwell et al., 2013), but includes updated geophysical observations for the Ellsworth Mountains (Napoleoni et al., 2020), Recovery Basin (Paxman et al., 2018), Totten Glacier (Greenbaum et al., 2015), and Amery Ice Shelf (Galton-Fenzi et al., 2008), and a new interpolation of near-grounding-line topography. The ice surface elevation from Bedmap2 is used to provide a stable initial configuration of the ice sheet, with grounded ice thickness calculated by differencing the new topography and ice surface elevation. The distribution of geothermal heat flow is based on an analysis of airborne magnetic data (Martos et al., 2017).

We use a horizontal grid resolution of 20 km and a vertical resolution of 30 m. The horizontal resolution is relatively coarse, but because we are simulating a full glacial cycle in an ensemble, using a higher resolution is computationally prohibitive. The vertical resolution is relatively fine although we note that increasing this further would likely result in better resolution of the temperate ice layers at the base of the ice sheet (Pittard, 2016; Albrecht et al., 2020a).

2.3. Model parameters

Our approach to parameterisation and use of an ensemble approach is partly driven by the findings of Phipps et al. (2021) who used PISM to model the present-day Antarctic ice sheet and showed that the co-dependence of parameters precludes choice of a single optimal set of parameter values. PISM has a large number of parameters and fully varying all of them in an ensemble would be unfeasible given our available computing resources. Instead, we used initial testing and guidance from the literature [e.g., Albrecht et al., 2020a; Martin et al., 2011; Phipps et al., 2021; Pittard et al., 2017] to set some parameters to fixed values (Table 1) and identify a subset of five key parameters that exert a strong control on the evolution of the numerical model. We varied these five parameters in our ensemble, namely the SIA enhancement factor (SIAE), the SSA enhancement factor (SSAE), the lower till angle (LPHI) in the piecewise linear relationship, slipperiness of the grounding line (SGL) - collectively referred to as the glaciological parameters - and mantle viscosity. In addition we used a range of climate scenarios to force the model.

The four glaciological parameters were chosen because they control ice flow in different regions of the ice sheet. The SIAE

Table 1
PISM parameters and forcing used in this study, including a comparison to those used in (Albrecht et al., 2020a, 2020b)). Elements in bold were varied as part of our model ensembles.

Parameter (units)	This Study	Albrecht et al. (2020A, B)
Topography	DUbmap	Bedmap2
Geothermal Heat Flux (W m^{-2})	Martos et al., (2017)	Martos et al., (2017)
Horizontal Resolution (km)	20	16
Vertical Resolution (m)	30	20
SIAE	**Ensemble Member**	Ensemble Member
SSAE	**Ensemble Member**	0.6
Pseudo-Plastic Quotient (PPQ)	0.75	Ensemble Member
Till Overburden Pressure	0.03	0.04
Till Decay Rate (mm $year^{-1}$)	1	1
Till Angle Parametrization	Piecewise linear parameterisation	Inversion based
Upper Phi Till Angle (°)	35	Inversion based
Lower Phi Till Angle LPHI (°)	**Ensemble Member**	Inversion based
Upper Phi Elevation (m)	1000	Inversion based
Lower Phi Elevation (m)	−500	Inversion based
Till Depth (m)	2	2
Climate	**Ensemble Member**	Similar to Scenario 1
Sea Level	Spatially varying from Sea Level Solver (Supplementary Data)	ICE-6G_C reconstruction
Overturning Strength (m^6 s^{-1} kg^{-1})	1.0×10^6	1.0×10^6
Effective Turbulent temperature exchange Velocity (ms^{-1})	2.0×10^{-5}	2.0×10^{-5}
Eigen Calving constant, K (m s)	5×10^{17}	1×10^{17}
Calving Thickness value (m)	Spatially varying (75–175)	75
Mantle Viscosity (Pa s)	**Ensemble Member**	**Ensemble Member**
Slipperiness of Grounding Line SGL (%)	**Ensemble Member**	Advancing ice sheet is saturated

directly modifies the rate of deformation in the interior of the ice sheet where there is little to no sliding. The SSAE modifies ice flow within the ice shelves by changing the amount of upstream buttressing, as well as enhancing grounded ice flow where sliding is occurring. LPHI modifies where and how extensively basal sliding occurs. Lastly, the SGL parameter modifies the basal resistance adjacent to grounding lines, which influences the rate of grounding line movement and the extent to which ice shelves buttress the upstream flow.

PISM has an inbuilt coupled viscoelastic deformation model, based on Lingle and Clark (1985) and Bueler et al. (2007). Including solid Earth deformation within an ice sheet model is important because it controls aspects of advance and retreat that will not be reflected in a fixed-bed model (Van den Berg et al., 2008). We use the elastic module with the default flexural rigidity value within PISM (5×10^{24} Nm) and three mantle viscosity values that broadly represent the range of mantle viscosity values inferred for Antarctica (Whitehouse et al., 2019).

2.4. Climate forcing

We use four climate scenarios within our ensemble approach (S1–S4; see Table 2). Each scenario defines four time-varying climate indices that are used to drive various sub-models within PISM. The four climate indices are surface mass balance, ice surface temperature, practical ocean salinity, and potential ocean temperature. Time-varying continental mean values for each index are shown in Fig. 1. We proceed by describing the requirements of the PISM sub-models and then the construction of the four climate scenarios.

2.4.1. PISM sub-models

Climate forcing in PISM is controlled by three sub-models: surface, ocean, and sea level. The surface (atmospheric) sub-model requires input of time-varying 2D spatial fields of surface mass balance (SMB), ice surface temperature, and ice elevation. Specifically, spatial fields of SMB and ice surface temperature are prescribed for an a priori time-evolving ice sheet surface (the reference surface). As the ice sheet thickens or thins during a model simulation, perturbations to the prescribed SMB and ice surface temperature are determined using empirically derived linear lapse rates that describe how temperature varies with elevation (8.2 °C/km) and how SMB varies with temperature (Dome Fuji, 4.9%/°C (Frieler et al., 2015), or EDML, 6.3%/°C (Mulvaney, Private Communication)).

The ocean sub-model of PISM (Reese et al., 2018), requires input of time-varying 2D spatial fields of practical salinity and potential temperature at the depth of the continental shelf. These input fields are used to drive a box-model that calculates the rate of basal melt on the underside of ice shelves in 18 sub-regions around the coast of Antarctica (Fig. 2a).

The sea level sub-model requires input of a time-varying 2D spatial field of sea surface height. These fields are generated using a sea-level solver (Milne and Mitrovica, 1996) in combination with

Table 2
Data sources used to create the climate forcing scenarios.

Name	Ice core	Paleoclimate model	Elevation lapse rate surface elevation	Deglacial history for sea level sub-model
S1	Dome Fuji (Watanabe et al., 1999)	RACMO v2.3 (van Wessem et al., 2014) with a cold saline ocean	Bedmap2	W12 (Whitehouse et al., 2012a, 2012b)
S2	EDML (Robert Mulvaney, personal communication)	PMIP3-MRI-CGCM3 (Braconnot et al., 2011)	ICE-6G_C (Argus et al., 2014)	ICE-6G_C (Argus et al., 2014)
S3	EDML (Robert Mulvaney, personal communication)	HADCM3-W12 (William Roberts, personal communication)	W12 (Whitehouse et al., 2012a, 2012b)	W12 (Whitehouse et al., 2012a, 2012b)
S4	Dome Fuji (Watanabe et al., 1999)	PMIP3-MPI-ESM (Braconnot et al., 2011)	ICE-6G_C (Argus et al., 2014)	ICE-6G_C (Argus et al., 2014)

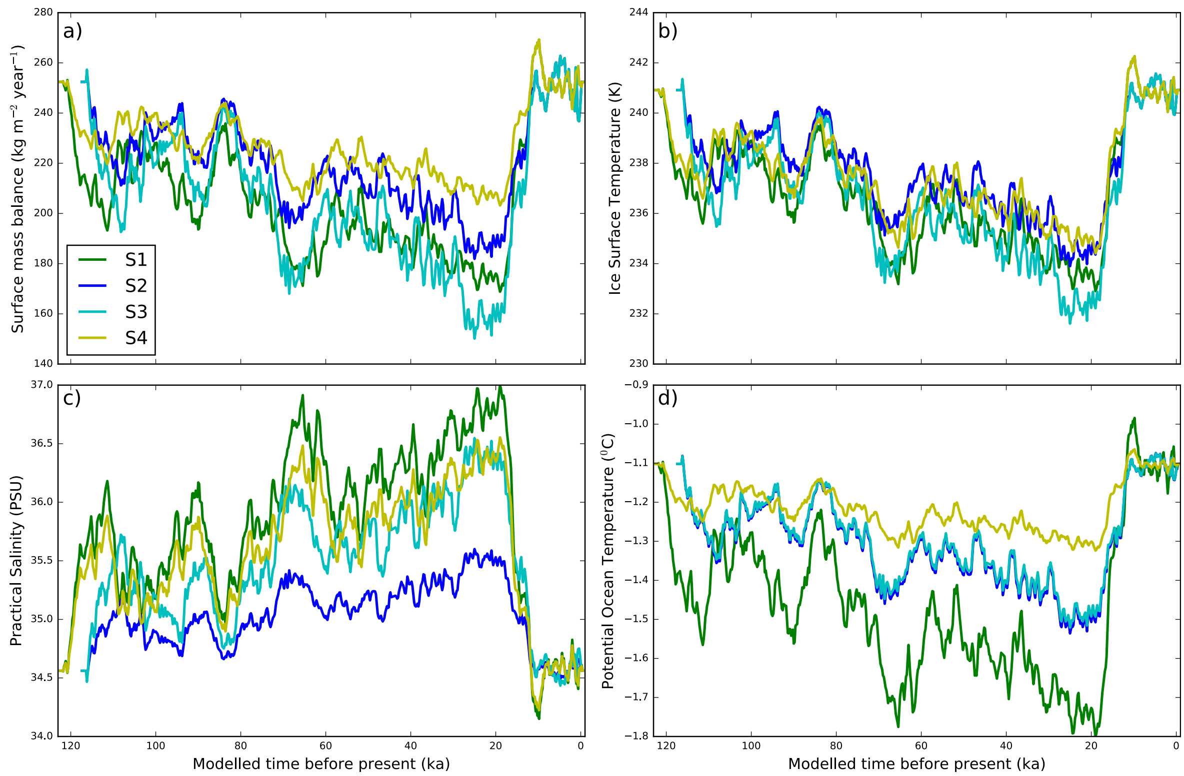

Fig. 1. Model climate forcings for the 120,000 year-long simulations. Panels show the average value over the continent of the four climate forcing parameters for atmosphere and ocean. Scenarios S1−S4 are explained in Table 2 and in the main text. (a) Surface mass balance, (b) Ice surface temperature below the firn layer, (c) Practical salinity and (d) Potential ocean temperature averaged over each basin at the local depth of the continental shelf, with depths greater than 1200 m using an average temperature between 800 m and 1300 m depth.

either the ICE-6G_C (Argus et al., 2014) or W12 (Whitehouse et al., 2012a) ice history model (see Table 2 and Supplementary Data). For each ensemble member, we use a sea surface height field that has been derived using the same upper mantle viscosity as is used in the PISM viscoelastic deformation model (i.e., a PISM simulation using a mantle viscosity of 1×10^{20} Pa s will be forced by a sea level field generated using an upper mantle viscosity of 1×10^{20} Pa s within the sea level solver).

2.4.2. Construction of climate scenarios

Each climate scenario is based on four components: (i) an ice core-derived temperature reconstruction, (ii) snapshots of climate model output, (iii) a reference ice surface, and (iv) an a priori deglacial model (refer to Table 2). The temperature reconstruction defines the temporal evolution of the four climate indices shown in Fig. 1. The climate model output is used to prescribe spatial fields of climate indices at four specific times (defined in discussion of ice core records below): the Last Interglacial (LIG), the Last Glacial Maximum (LGM), the start of the Holocene (HOL), and the present-day (PD). The reference surface provides a baseline for the calculation of temperature and SMB perturbations as the simulated ice sheet thickens or thins. Lastly, the a priori deglacial model defines the sea-level forcing at the grounding line of the ice sheet. Details of the specific components used in scenarios S1−S4 are listed in Table 2. We chose the two PMIP models (S2 and S4) based on their relative difference in atmospheric and ocean forcing (Fig. 1), as well as ensuring realistic climatic means (i.e, that the ocean was colder during the LGM than present day). The third model (S3) followed the methods of PMIP but utilised the W12 (Whitehouse et al., 2012a) ice sheet history (William Roberts, personal communication) to provide a contrast on the dependence of the a priori deglacial model.

A scaling approach is used to define the spatio-temporal evolution of climate indices between the climate snapshot times (LIG, LGM, HOL and PD). These times are defined according to specific events in the chosen temperature reconstruction. We use two temperature reconstructions, one based on the Dome Fuji ice core record (Watanabe et al., 1999) (S1 and S4) and one based on the EPICA Dronning Maud Land (EDML) ice core record (Robert Mulvaney, personal communication) (S2 and S3). The location of the two ice cores are shown on Fig. 3, along with a number of place names used throughout the manuscript. LIG is defined as the time at which temperature first dropped below the present-day temperature at the end of the Last Interglacial. The main experiment is initiated at this time, resulting in a simulation length of 124,000 years when forced by the Dome Fuji record and 118,600 years when forced by the EDML record. LGM is defined to be the time of the coldest temperature in the proxy record (19.2 ka for Dome Fuji, 21.2 ka for EDML), HOL is defined as the first time the temperature returns to the present-day temperature after the glacial period (11.8 ka for Dome Fuji, 11 ka for EDML), and PD is defined as AD 2000.

For climate scenarios S2−S4 the spatio-temporal evolution of the four climate indices is determined as follows. Spatial difference fields are calculated for each climate index for the epochs LIG-to-LGM and either LGM-to-HOL (temperature and SMB fields) or LGM-to-PD (ocean properties). The spatial fields are then divided by the net surface temperature change over the relevant period, as defined by the chosen temperature reconstruction, yielding a map of how each climate index varies per degree of surface temperature change during that period. Finally, the temperature reconstruction is used to modify the spatial climate index fields smoothly through time. The temporal resolution used in the climate forcing was 200

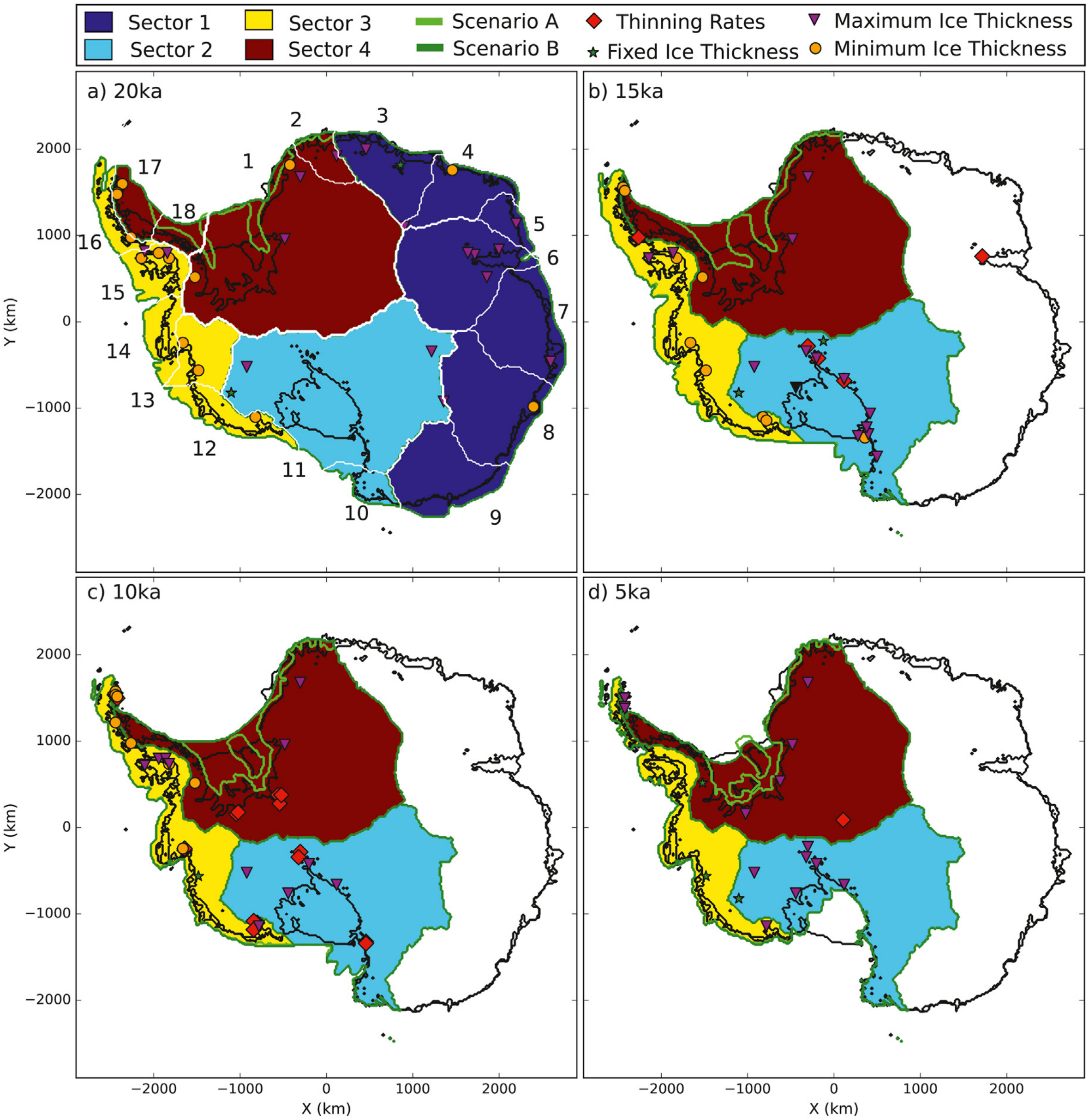

Fig. 2. Map of sectors and location of constraint data. The reconstructed grounding line positions and the onshore constraints for different timeslices are shown: (a) 20 ka, (b) 15 ka, (c) 10 ka, and (d) 5 ka. Fig. 2 (a) outlines the Antarctic ice sheet drainage basins (modified from Zwally et al., (2012), see supplementary information) which are combined into four distinct regions of Antarctica: Sector 1 (East Antarctica, Basins 3–9 in Zwally et al., (2012), Sector 2 (Ross Ice Shelf, Basins 10–11, Cyan), Sector 3 (Amundsen and Bellinghausen Seas, Basins 12–16, Yellow) and Sector 4 (Weddell Sea, Basins 17–18 and 1–2, Red). Two grounding lines are plotted for the RAISED reconstructed grounding lines: Scenario A (light green) and Scenario B (dark green). The discrete data points are: thinning rates (red diamond) (Small et al., 2019), and from the RAISED reconstruction we show maximum ice thickness (magenta triangle), minimum ice thickness (orange circle) and fixed thickness estimate (green star). Note that the RAISED reconstruction had insufficient data to reconstruct grounding line positions for East Antarctica after the 20 ka timeslice. The spatial projection used here and hereon is Antarctic Polar Stereographic (EPSG3031).

years which was consistent with the Dome Fuji record. In all cases, LIG and (where relevant) HOL spatial fields are defined to be the same as PD spatial fields, which are defined by RACMO2.3 (van Wessem et al., 2014) and ocean observations (Schmidtko et al., 2014). LGM spatial fields are derived from climate model output (see Table 2 for details). For the period between HOL and PD, temporal variations in surface temperature and SMB are driven by changes to the elevation of the reference ice surface and determined using the lapse rates quoted in section 2.4.1. For the 1000 years beyond present day (see section 2.2) we force the model using PD climate conditions.

The reference ice surface evolves through time and is used as a baseline for calculations of perturbations to temperature and SMB that arise due to changes in the surface elevation of the ice sheet. Similar to above, the temperature reconstruction defines how the reference ice surface evolves through time, with values scaled between present-day ice surface elevations (derived from Bedmap2; Fretwell et al. (2013)), and an a priori LGM ice sheet configuration (see Table 2).

Unlike scenarios S2–S4, which draw on climate model reconstructions of conditions during the last glacial period, scenario S1 is based on the scaling of modern climate index fields throughout the whole of the model simulation. The Dome Fuji temperature reconstruction is used to define the time-dependent shift that is applied to the present-day surface temperature field and the scaling of the present-day SMB field (4.9% increase per

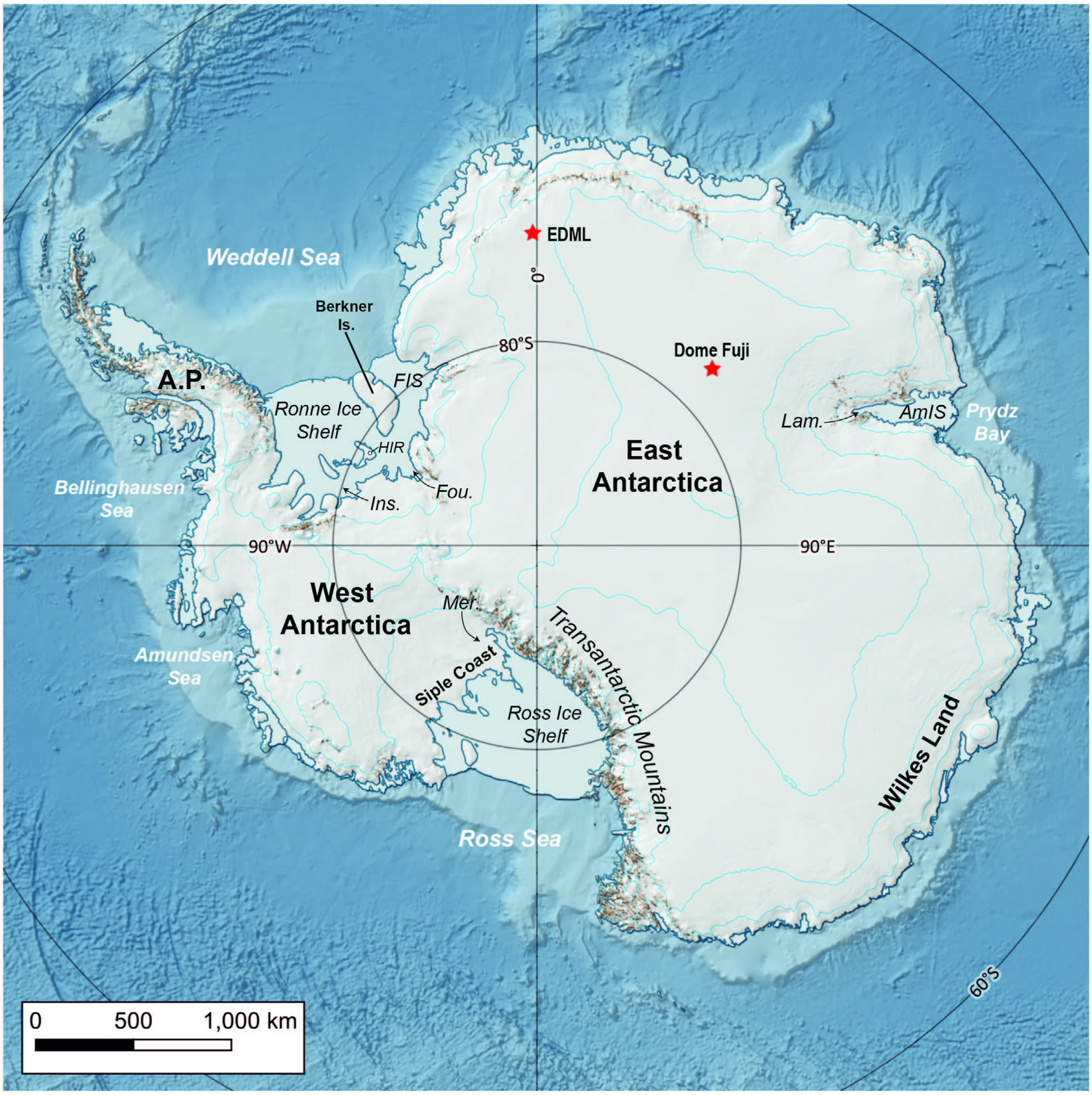

Fig. 3. Place names used through the manuscript. The ice core sites used to create the climate forcing scenarios are indicated as a red star; EDML = EPICA Dronning Maud Land. A.P. = Antarctic Peninsula, FIS = Filchner Ice Shelf, AmIS = Amery Ice Shelf, HIR = Henry Ice Rise, Lam. = Lambert Glacier, Fou. = Foundation Ice Stream, Ins. = Institute Ice Stream, Mer. = Mercer Ice Stream.

degree of warming). A reference ice surface (Bedmap2) is still used, to permit the calculation of elevation-driven perturbations to the temperature and SMB fields. Ocean conditions are scaled between modern and LGM conditions, with the LGM ocean assumed to have a uniform temperature of −1.8 °C and salinity 37 PSU, based on pore water measurements from sediments in the Pacific, Atlantic and Indian Oceans, which show seawater temperatures were within error of freezing, and salinities were 1–2.5 PSU saltier (Adkins et al., 2002).

3. Scoring methods

We have developed a new scoring method to assess the performance of an ensemble of Antarctic deglacial reconstructions with respect to geological observations. The method is designed to be used on large model ensembles where visual inspection of every member is unfeasible. It aims to eliminate simulations which do not meet set criteria (sieves) while providing relative measures (scores) and rankings of performance between those ensemble members which pass the sieves. We focus on identifying the deglacial histories that best represent our knowledge of the ice sheet history relative to the other members of the ensemble; the best ten simulations will then undergo further investigation. Our primary focus is on using observations of palaeo ice extent (area) and ice thickness through time, because we ultimately intend to use the deglacial history as an input for GIA modelling. The approach of scoring a whole ensemble can also provide insights by identifying modelled behaviour that shows consistent mismatches - in space or time - with the geological data.

3.1. Geological data

Our knowledge of the evolution of the Antarctic Ice Sheet is mainly guided by geological observations of ice extent and ice thickness. Large compilations of these observations have been used to develop or constrain a wide range of deglacial models [e.g., Whitehouse et al., 2012a, Briggs et al., 2014]. Such observations have been reviewed elsewhere [e.g. Bentley et al., 2014] so here we only briefly outline the main types of observation with a focus on those we use in our scoring algorithm. Marine-based observations come from analysis of marine sediment cores and geophysical survey data. Their main constraining power lies in determining the former lateral extent of the ice sheet margin (e.g., based on geomorphology) and in determining the timing of grounding line retreat (e.g. by dating of organic matter associated with sub-glacial sediments). Geophysical data such as shallow seismic surveys and high-resolution seabed surveys reveal landforms and stratigraphy that record where former grounding lines were located, where paleo-ice streams formed, and where and when large calving events occurred [e.g.,Hodgson et al., 2019, Arndt et al., 2020]. The timing of ice sheet retreat is usually determined from radiocarbon dating of changes in sedimentation regime in cores [e.g. Larter et al., 2014]. Because of the general scarcity of organic material within glacial sediments dates are usually obtained from horizons that are located below and, more commonly, above sub-glacially deposited material and were thus deposited some (unknown) time before or after ice sheet retreat. Such dates can only provide maximum or minimum constraints on grounding line retreat and the timing of deglaciation. Marine constraints are therefore usually of the form: horizontal position and (limiting) date.

Terrestrial observations are generally limited to the <1% of Antarctica that is ice free and where the geological record of ice sheet fluctuations is preserved. The main constraining power of terrestrial observations is to determine upper limits of the former ice surface and the timing of thinning. Numerous studies have combined geomorphological observations of evidence for former ice sheet presence on nunataks with cosmogenic surface exposure dating of glacial deposits along vertical transects to determine the timing and rate of thinning through time [e.g., Stone et al., 2003, Bentley, 2010, Mackintosh et al., 2011, Spector et al., 2017, Small et al., 2019]. Geomorphological evidence of the former vertical extent of the ice sheet is usually provided by the height of lateral moraines and/or weathering limits [e.g., Bentley, 2010]. Cosmogenic surface exposure ages can, in principle, directly date glacial deposits however given the potential for erosion and/or inherited nuclides they are commonly interpreted as minimum constraints on the timing of deglaciation. Similarly a cosmogenic exposure age from the summit of a nunatak only provides a minimum for former maximum ice sheet thickness; prior to that date the ice sheet may have been thicker but by an unknown amount. Additionally, a small number of constraints on former ice thickness – especially in the interior - can additionally be derived from ice core measurements (Martinerie et al., 1994; Werner et al., 2018; Bradley et al., 2013). These can be important to provide past thickness constraints for large expanses of the ice sheet where no nunataks exist. Terrestrial constraints therefore tend to be of the form: horizontal position, ice elevation/thickness and (limiting) date.

We use the compilation of paleo observations from the RAISED consortium (Bentley et al., 2014) supplemented by a recent compilation of ice thinning rates (Small et al., 2019) as the databases underpinning our scoring method (refer to Fig. 2). The RAISED reconstructions are focussed on four timeslices at 20 ka, 15 ka, 10 ka and 5 ka; a spacing of 5 ka was chosen by RAISED to provide a reasonable compromise between data availability and the needs of modellers. Due to two contrasting datasets for the past extent of ice in the Weddell Sea (Hillenbrand et al., 2014) the RAISED reconstruction provides two different scenarios (Scenario A and Scenario B) for the paleo extent of the ice sheet through time in this region. We score each simulation against both paleo-extent scenarios, with only the best scoring scenario being used to calculate the total score for each member. Terrestrial observations either provide an upper or lower bound on ice thickness or an estimate of the absolute elevation of the past ice surface. The thinning rates dataset provides information on: the onset of major deglaciation, the period over which thinning takes place, and the average thinning rate over this period, all of which can be scored against model output.

To investigate how well the deglacial reconstructions replicate the past extent of the ice sheet we define four distinct sectors of Antarctica by combining drainage basins (adapted from Zwally et al., 2012, Fig. 2a): the East Antarctic Sector (Sector 1, Drainage Basins 3–9), the Ross Sea Sector (Sector 2, Drainage basins 10–11), the Amundsen and Bellingshausen Seas Sector (Sector 3, Drainage basins 12–16) and the Weddell Sea Sector (Sector 4, Drainage basins 1–2, 17–18). We calculate the simulated area of the palaeo grounded ice sheet for each of the four sectors and each of the four palaeo time-slices. Thinning rate observations are assigned to the closest palaeo time-slice. However, if the period of thinning exceeds 5000 years, the observation is assigned to all relevant time-slices. Scores are calculated for each sector as well as the whole ice sheet.

To score the performance of the ensemble members against present-day observations we use the Durham University bedrock map (DUbmap, see Supplementary Data) in conjunction with the Bedmap2 surface elevation data-set (Fretwell et al., 2013). The 18 drainage basins of the ice sheet (Fig. 2a) are used to calculate the area of the present day ice sheets and to define boundaries for the oceanic sub-model within PISM (Reese et al., 2018).

The data-set to be used in the scoring method can be visualised in Fig. 2. Sector 1 has very limited constraint data for time-slices other than the 20 ka time-slice (Bentley et al., 2014; Mackintosh et al., 2014), and full grounding line reconstructions are not available for the sector for the 15 ka, 10 ka and 5 ka timeslices. With the exception of some ice core measurements at 20 ka, ice thickness constraints are limited to either mountain ranges or coastal regions.

3.2. *Scoring approach*

3.2.1. *Present day sieves*

We define two sieves that are used to filter our ensembles: present-day ice volume above flotation and total area of present-day ice shelves (Fig. 4). For a simulation to pass these sieves it needs to have a present day volume which is within −1 to +3 m SLE of the observed, and an ice shelf area that is at least 75% of the observed (Fig. 4). These sieves were chosen to identify those simulations which best-approximated the present day ice sheet and deglaciated sufficiently for use in solid Earth modelling. We allowed for a bias towards slightly larger present-day ice volume because models with relatively coarse resolution are unable to resolve narrow ice outlets or narrower ice shelves, leading to less evacuation of ice and subsequent higher total volume. We decided against using palaeo-sieves, such as the sea-level contribution during the last interglacial (Briggs and Tarasov, 2013; DeConto and Pollard, 2016), because uncertainty in Antarctica's contribution to global sea level (Edwards et al., 2019) and in the contemporaneous climate make this a challenging time interval from which to use paleo constraints.

3.2.2. *Scoring against geological data*

The simulations that pass the present-day sieves are then scored numerically against the geological data that record palaeo ice extent. We design the scoring method around the palaeo and present-day time-slices: 20 ka, 15 ka, 10 ka, 5 ka and 0 ka. For each time-slice a deglacial reconstruction will receive a score between

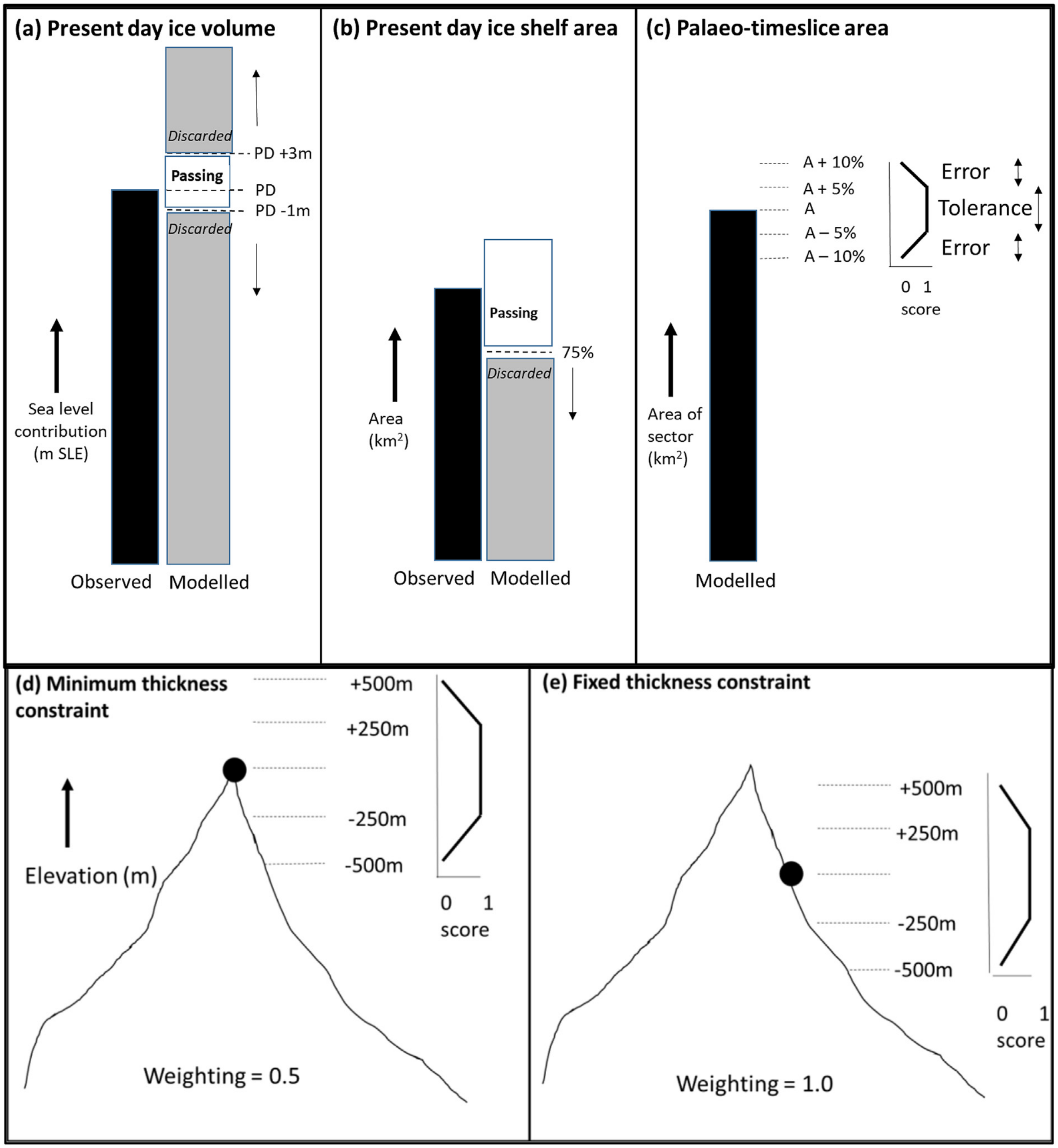

Fig. 4. Schematic of sieves and scoring methodology. (a) Use of a sieve for present-day (PD) size of the ice sheet (calculated as volume above flotation, and expressed in metres sea level equivalent (SLE)). Model runs that exceed PD contribution by > 3 m or under-predict by > 1 m are discarded. (b) Sieve for present day ice shelf area. Runs which reproduce a total ice shelf area of <75% of the observed area are discarded. (c) Concepts of tolerance and error for scoring model runs compared to palaeo-data. Modelled values within a certain range (tolerance) of the observed value are assigned a score of 1, and this declines to a score of zero over a range (error) beyond the tolerance limit. (d) Scoring of ice thickness measurements on a nunatak showing a down-weighting of minimum geological constraints, and (e) a weighting of 1 for fixed values of former ice thickness.

0 and 1 with a score of 0 matching none of the available observations and 1 matching all observations. It is improbable that any simulation will score the maximum, so the focus of this method is on the comparison between scores within this range.

For the purpose of scoring we use two terms: Tolerance and Error (Fig. 4). When comparing a simulation to observations we define a tolerance within which a simulation will score 1 if it is sufficiently close to the observation. This is to recognise that there is inherent uncertainty in both the numerical simulations and the observation itself, so to expect a model simulation to be able to reproduce an observation exactly is unreasonable. Fig. 4c shows that, for example, if the area of a sector is simulated within ±5% of the observed geological evidence of palaeo-extent then in our scheme it will score 1. To avoid abrupt steps in scoring, when modelled parameters are just inside or outside our defined tolerance, we also define a range (termed here, 'error') for each parameter where the score reduces in a linear fashion from 0 to 1. For example, in the case of the palaeo-area of a sector this error is set to an additional 5% beyond the tolerance (Fig. 4c). As a result, model simulations with parameters outside ±10% of the observed value will score 0, those within 5–10% will score between 0 and 1 and those within 5% will score 1. In the next section we discuss the parameters that we score, the ways that they are scored against observations, and the weightings given to different scores.

3.2.3. Scoring simulations of grounding-line position

To assess a simulation's ability to reproduce the grounding line position through time, an analytical method is needed. Whilst visual comparison of grounding lines is relatively easy to do, in an ensemble of simulations this becomes impractical, and can lead to focus on fine-scale differences rather than the ability of the ensemble to reproduce broad patterns of grounding-line change. Our approach takes advantage of the synthesis work carried out by the RAISED consortium to reconstruct grounding line positions that are more accurate than those provided by individual datapoints of variable data quality. For our scoring method we use the paleo-area of each sector as a key metric to assess simulated grounding line positions. We calculate the paleo-area for each sector (Fig. 2) at each of the RAISED time-slices. In the Weddell Sea sector we compare the simulated paleo-area with both paleo-extent scenarios in the RAISED dataset. This provides us with a comparison that can be used to quickly determine how accurately each simulation replicates grounding line migration through time. The disadvantage of this approach is that if the ice sheet advances in some regions, and retreats in others, it could bias our results. To reduce this risk, we assess each of the four sectors individually rather than score the whole ice sheet area: each simulation is scored by comparing the modelled area of grounded ice in each of the four sectors with the observed palaeo ice sheet area in each timeslice. For 20 ka we are able to score all 4 sectors but in the RAISED compilation our Sector 1 (East Antarctica) does not have sufficient data to compile grounding line positions for the 15, 10 and 5 ka time slices (Bentley et al., 2014) and so in these cases we only score the three other sectors. Both Scenario A and Scenario B are scored in the Sector 4 (Weddell Sea sector), with the best scenario automatically selected in the total score.

Each sector is weighted equally when calculating the total score for each time slice (4 sectors for 20ka, 3 sectors for 15, 10 and 5ka). For the 0 ka time slice the modelled area is calculated for each drainage basin (1–18; Fig. 2a) and weighted relative to the largest drainage basin within each sector.

3.2.4. Scoring simulations of paleo ice sheet thickness

The four different types of palaeo ice thickness observations (maximum ice extent, minimum ice extent, fixed thickness measurement, and thinning rate; Table 3) are scored together. For the RAISED single point observations, a tolerance of 250 m and an error of 250 m is used. This range was chosen because it represents a 5% error on a possible 5000 m ice thickness maximum. The numbers are consistent with uncertainties in observations of ice surface height close to nunataks (e.g. due to windtails, wind scoops, and other minor fluctuations in ice sheet surface). For the thinning data, which already reflects a summary of multiple datapoints and includes an uncertainty distribution (Small et al., 2019), a simulation that replicates the observed thinning rate within the 2 sigma error is assigned a score of 1.

Table 3
Types of palaeo ice thickness data and the number of observations per timeslice.

Data Types	20ka	15ka	10ka	5ka	Total
Thinning Rates	0	0	11	18	29
Maximum Ice Extent	16	10	12	0	38
Minimum Ice Extent	3	3	2	3	11
Exact Ice Extent	18	14	12	14	58
Total	37	27	37	35	136

Each data point within a sector is weighted by the complexity of the local topography and whether it is a fixed thickness measurement or an upper/lower bounding constraint. This first weighting is motivated by recognising that in highly complex regions of topography, the features measured by the observations are below the resolution of the model and less reflective of the regional ice sheet configuration. In essence, we want to up-weight observations that lie close to large ice streams, and down-weight observations in complex mountainous ice caps. The weighting is necessary because of the challenges of comparing field geological data to model grids [e.g., Mas e Braga et al., 2021; Whitehouse et al., 2012a]. To determine the topography weighting, we calculate the standard deviation (s.d.) of topography (1 km resolution) within the grid cell (20 km × 20 km) that contains the data point. For s.d. < 200 m a weighting of 1 is used, for s.d. between 200 and 380 m the weighting decreases linearly to 0.1, and for s.d. > 380 m a weighting of 0.1 is used. This results in a spread of weights of 46% between 0.1 and 0.4, 15% between 0.4 and 0.7 and 39% between 0.7 and 1. Fixed measurements are assigned an additional weighting of 1 (Fig. 4e), while measurements that only provide a bound (e.g. ice thickness change was 500 m or more) are down-weighted by 0.5 (Fig. 4d), because comparison to a maximum/minimum value implicitly provides less constraint than comparison to a fixed value.

For the 0 ka time slice we score each simulation according to how well it reproduces present-day ice surface elevations. We calculate the normalised root-mean-square-error, comparing simulated and observed ice surface elevations. The normalisation is carried out over a range of 5000 m, with a tolerance of 5% (250 m) and error of 250 m.

3.2.5. Treatment of temporal error

Uncertainty associated with dating is considered in our scoring scheme. For the RAISED reconstructions, palaeo-extent data were synthesised at 5 ka timeslices, deliberately incorporating a range of data to come up with estimates of grounding line positions at those timeslices. This approach necessarily involved a degree of binning data into age groups and in some cases interpolation between dated points [e.g., Larter et al., 2014]. To allow for the interpolation of those datapoints we use a tolerance of 2.5 ka when comparing model output and geological constraints at each of the 20, 15, 10 and 5 ka RAISED timeslices.

The 2.5 ka tolerance is applied independently for all data because deglaciation was not necessarily synchronous between sectors (Bentley et al., 2014). Model output is considered every 100 years. This means that a simulation may score highest at 21 ka in one sector and 19 ka in another. Both these scores would be included in the score for the 20 ka timeslice. A lower temporal tolerance is used for the 0 ka time slice. We recognise the uncertainty in palaeoclimate and modelled trajectory of the sheet leading into the present day modelled extent, and so allow a tolerance of 1 ka for this timeslice. For each simulation, the scores from the five time slices are averaged to determine the total score.

4. Ensemble 1

We divide our modelling experiments into two ensembles. The first ensemble focuses on the broader scale influences on ice sheet evolution such as climate and mantle viscosity. We also test a range of glaciological parameters. The aim of this ensemble is to identify optimum choices for climate and mantle viscosity, and to provide guidance on where the glaciological parameter space should be sampled in greater detail in the second ensemble. The ensemble uses the four different climate forcing scenarios (S1- S4), three choices of mantle viscosity and two different values for the

Table 4
Summary of parameter combinations for Ensemble 1. For each choice of SGL the other three glaciological parameters only take one of the two values shown in the columns directly below. For example, for 50% SGL the ensemble only includes runs with SIAE of 2.5 or 3

Ensemble Member	Values		No. of Models
Climate Scenarios	S1, S2, S3, S4		4
Mantle Viscosity (Pa s)	5×10^{19}, 5×10^{20}, 1×10^{21}		3
Glaciological Parameters			
SGL	50%	75%	2
SIAE	2.5, 3	2,25	2
SSAE	1, 1.3	0.7, 1	2
LPHI (°)	3, 5	5,7	2
Total Models			192

slipperiness of the grounding line (SGL) parameter. Each of the two different SGL members are combined with a further three corresponding glaciological parameters (SIAE, SSAE, PHI), with two values used in conjunction with each SGL value. The total number of simulations is 192 (Table 4).

4.1. Ensemble 1 results

When the 192 simulations in Ensemble 1 are scored and sieved, 55 of the 192 simulations pass the sieve tests (Fig. 5). The passing simulations' total scores ranged from 0.46 to 0.78. The lowest scoring time slice is 0 ka, while for the top simulations the highest scoring time slice was 15 ka. The sieve for modelled present-day ice volume was the primary reason that the simulations failed, with the majority (95 of 97 failed) of these caused by the simulations not deglaciating sufficiently to be considered for further analysis.

The passing simulations demonstrate a variety of different behaviours with respect to ice-sheet expansion and deglaciation (Fig. 5). The LGM volume difference to present day ranges between 2.32 m and 14.39 m sea-level equivalent (ice volume above flotation, calculated relative to each ensemble member's own present day ice sheet volume, Fig. 5). Rapid deglaciation, hence rapid volume change, starts at approximately 15 ka for most simulations, but the rate of deglaciation varies across the simulations. Several simulations predict that the ice sheet was smaller than present during the Holocene, and that total ice volume has increased during the last few thousand years. There is a clear relationship between the mantle viscosity value used and the volume of the ice sheet, with a

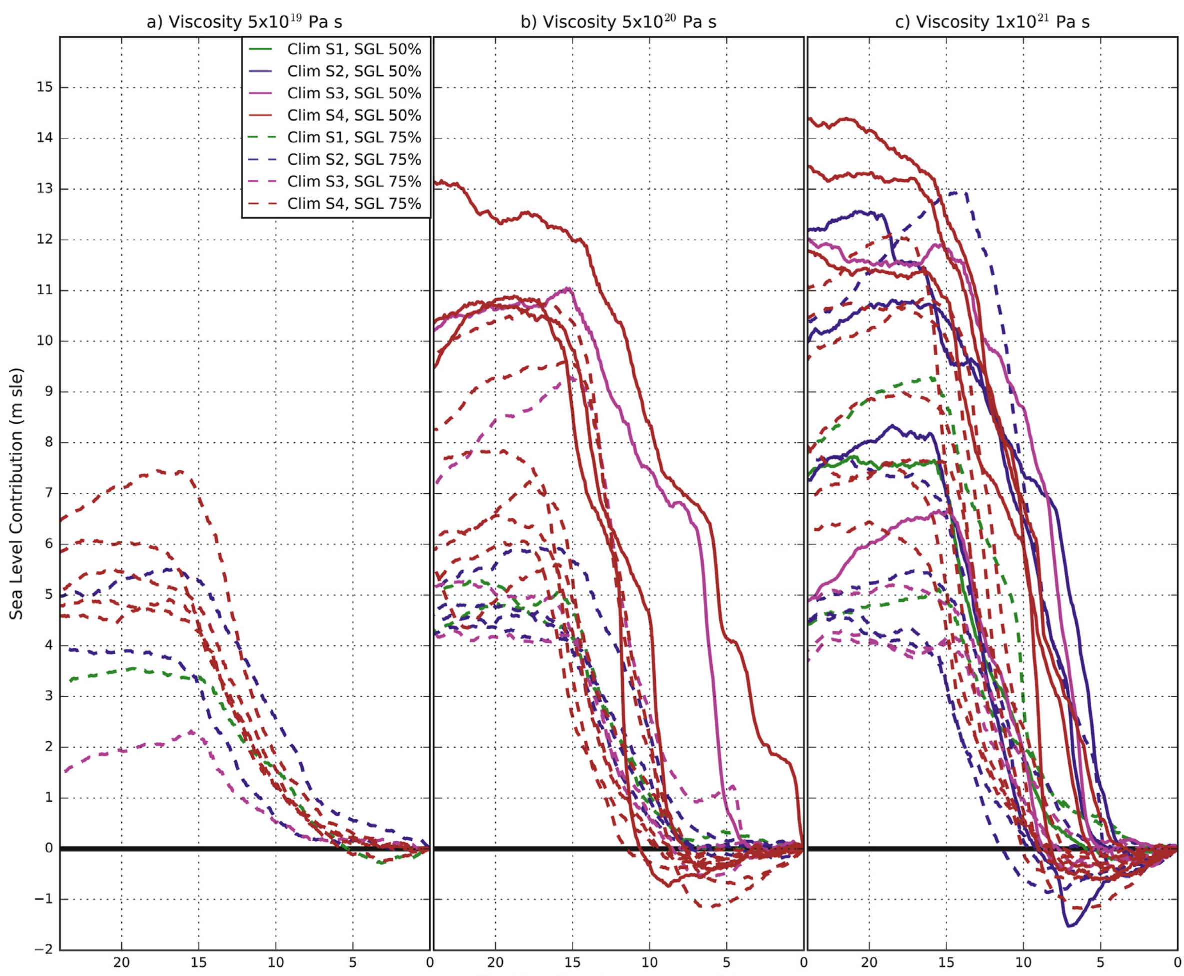

Fig. 5. The sea level contribution (m sle) through time of the 55 simulations from Ensemble 1 (out of a total of 192) which passed the sieves (see Table 5 for details). The sea level contribution is expressed relative to present and is calculated relative to each simulation's best scoring present day volume and is calculated as ice volume above flotation. Passing simulations are classified according to climate scenarios, slipperiness of the grounding line (SGL), and plotted for different mantle viscosities: (a) mantle viscosity of 5×10^{19} Pa s, (b) mantle viscosity of 5×10^{20} Pa s and (c) mantle viscosity of 1×10^{21} Pa s. The legend on panel (a) applies to (a)–(c), noting that not all model combinations are represented in each plot.

stiffer mantle leading to a greater modelled change in ice sheet volume between the LGM and the present day (Fig. 5). The 55 simulations that passed the sieves tend to score highest and with greatest number of passing simulations for climate S4, and viscosity 1×10^{21} Pa s (Table 5). For the grounding line slipperiness parameterisation, the highest scoring passing simulations are where SGL = 50% but it is notable that a significantly higher number of passing simulations have SGL = 75%. We next explore the use of the parameters consistently underpinning the best-scoring simulations to provide robust parameter choices for Ensemble 2.

4.1.1. Assessment of climate scenarios

We sampled four different climate scenarios in our ensemble. Of the four scenarios, S1 scored the lowest (0.57), with only 6 passing simulations. This is unsurprising, as it used a PD spatial field as the basis of its evolution through time, rather than a Global Climate Model (GCM) evolving with the ice sheet.

For the other scenarios, S2 (score of 0.59, 14 passing simulations), S3 (0.63, 10), and S4 (0.65, 25), we compare the LGM configuration of the top-scoring simulations (Fig. 6a and b). The scenarios with less surface mass balance input (S2 and S3; Fig. 1) generate top-scoring simulations with a thicker interior ice-sheet that is thinner at the coast relative to S4. Additionally, when comparing S2 to S4, it is evident that S2 was unable to produce an ice-sheet that advanced to the continental shelf in two of the three largest ice shelf regions of Antarctica (Fig. 6b) contrary to geological observations. This indicates that S4 distributes mass towards the coastline more efficiently than S2 or S3. When looking at the summary deglacial characteristics, the mean LGM Volume difference to PD (m SLE) is higher for S4 than the other scenarios (Table 5), but on average S3 and S4 take a similar time to deglaciate. Our results suggest that a scenario which produces a large ice sheet (by volume) that deglaciates relatively rapidly provides the best fit to the observations.

Given this and considering that the highest scoring climate scenario, S4, also had the greatest number of passing scenarios, we subsequently use this climate for Ensemble 2 (Section 5).

4.1.2. Assessment of mantle viscosity

The results indicate that using a mantle viscosity of 5×10^{19} Pa s does not lead to a good representation of the Antarctic Ice Sheet, with only 9 simulations passing the sieves, and the lowest average score (0.57) of the three values applied (Table 5). When using mantle viscosity values of 5×10^{20} Pa s and 1×10^{21} Pa s, the latter had slightly more passing simulations (26 vs. 20) and a slightly higher average score (0.63 vs. 0.62). Comparing the LGM configuration of the top-scoring simulations generated using 1×10^{21} Pa s and 5×10^{20} Pa s (Fig. 6c), there is relatively little difference in the distribution of ice thickness compared to the other parameters. There is a slight increase in ice thickness in the interior for the lower mantle viscosity, inverted towards the continental shelf where the higher viscosity had slightly higher ice thickness. Greater differences are evident during deglaciation, when variations in the rate of solid Earth rebound will influence ice dynamics via the control on water depth at the grounding line and beneath the ice shelf, with the latter determining whether the ice regrounds to form pinning points.

The smallest Holocene ice volume across Ensemble 1 is −1.52 m SLE for 1×10^{21} Pa s, −1.16 m for 5×10^{20} Pa s, and −0.3 m for 5×10^{19} Pa s (Fig. 5), suggesting that there is a connection between mantle viscosity and the ice sheet's propensity to retreat behind present-day grounding line positions. It has been suggested that during the Holocene, sections of the Antarctic Ice Sheet may have retreated behind their current grounding line positions before re-advancing over the last few thousand years (Bradley et al., 2015; Kingslake et al., 2018). This behaviour is reproduced in many of the simulations in Ensemble 1 and we explore it further when discussing the results of Ensemble 2 (Section 5).

Recent reconstructions are converging on an Antarctic Ice Sheet LGM volume on the order of 9.9 m ± 1.7 m SLE (Simms et al., 2019), which was best reproduced by simulations that assumed a mantle viscosity of 1×10^{21} Pa s. Given this, and with the slightly higher score for this group of simulations, we subsequently use 1×10^{21} Pa s to represent mantle viscosity in Ensemble 2.

4.1.3. Assessment of slipperiness of grounding line (SGL)

The results suggest that the SGL parameter exerts a strong control on LGM ice volume. On average, simulations that used an SGL value of 50% had a mean LGM volume difference of 10.98 m SLE, compared with 6.54 m SLE when the SGL parameter was set to 75% (Table 5). The higher LGM volume is associated with a significantly higher mean score (0.74) but fewer passing simulations (13 vs. 42). The only time slice in which an SGL of 75% scored better than an

Table 5
Statistics for the simulations in Ensemble 1 which passed the sieves. Each of the 55 passing simulations is reported under each of the three parameters sampled in ensemble 1. The chosen values of each glaciological parameter for Ensemble 2 are those with the highest average scores, namely Climate Scenario S4, Mantle Viscosity 1×10^{21} Pa s and Grounding Line Slipperiness of 50%. A range of summary deglacial characteristics are reported: the average timestep before PD at which LGM was reached (max ice volume), the mean LGM volume difference to PD is calculated as the difference (in m SLE) between the highest volume of a simulation between 22.5 ka to 17.5 ka, the average timestep before PD at which the Holocene minima was reached, and the highest scoring 0 ka time-slice between 1 ka and −1 ka. Mean deglaciation duration is a crude measure of time taken to transition from maximum volume to near-present ice sheet volume. Deglaciation duration is calculated as the time between the model timestep with maximum volume and the timestep when volume reaches modelled present-day volume for the first time. A model may reach a minimum volume several ka after it first reaches present-day volume for the first time (see Fig. 8a). The mean Holocene minimum volume difference is calculated relative to PD.

Values	No. of Passing Models	Average Final Score	LGM timestep before PD (ka)	Mean LGM Volume difference to PD (m SLE)	Mean Deglaciation Duration (kyr)	Mean Holocene Minimum timestep before PD (ka)	Mean Holocene Minimum Volume difference to PD (m SLE)
Climate Scenario							
S1	6	0.58	18.12	6.00	3.35	2.07	−0.10
S2	14	0.59	19.48	6.89	4.75	2.87	−0.31
S3	10	0.63	17.95	6.44	6.16	3.00	−0.22
S4	25	0.65	19.45	8.83	6.90	4.68	−0.38
Mantle (Pa s)							
5×10^{19}	9	0.58	19.59	4.90	2.63	1.40	−0.09
5×10^{20}	20	0.62	18.67	7.41	6.41	4.02	−0.28
1×10^{21}	25	0.64	19.13	8.66	6.50	4.11	−0.40
SGL (%)							
50.00	13	0.74	19.52	10.98	5.65	3.79	−0.43
75.00	42	0.59	18.89	6.54	5.89	3.58	−0.26

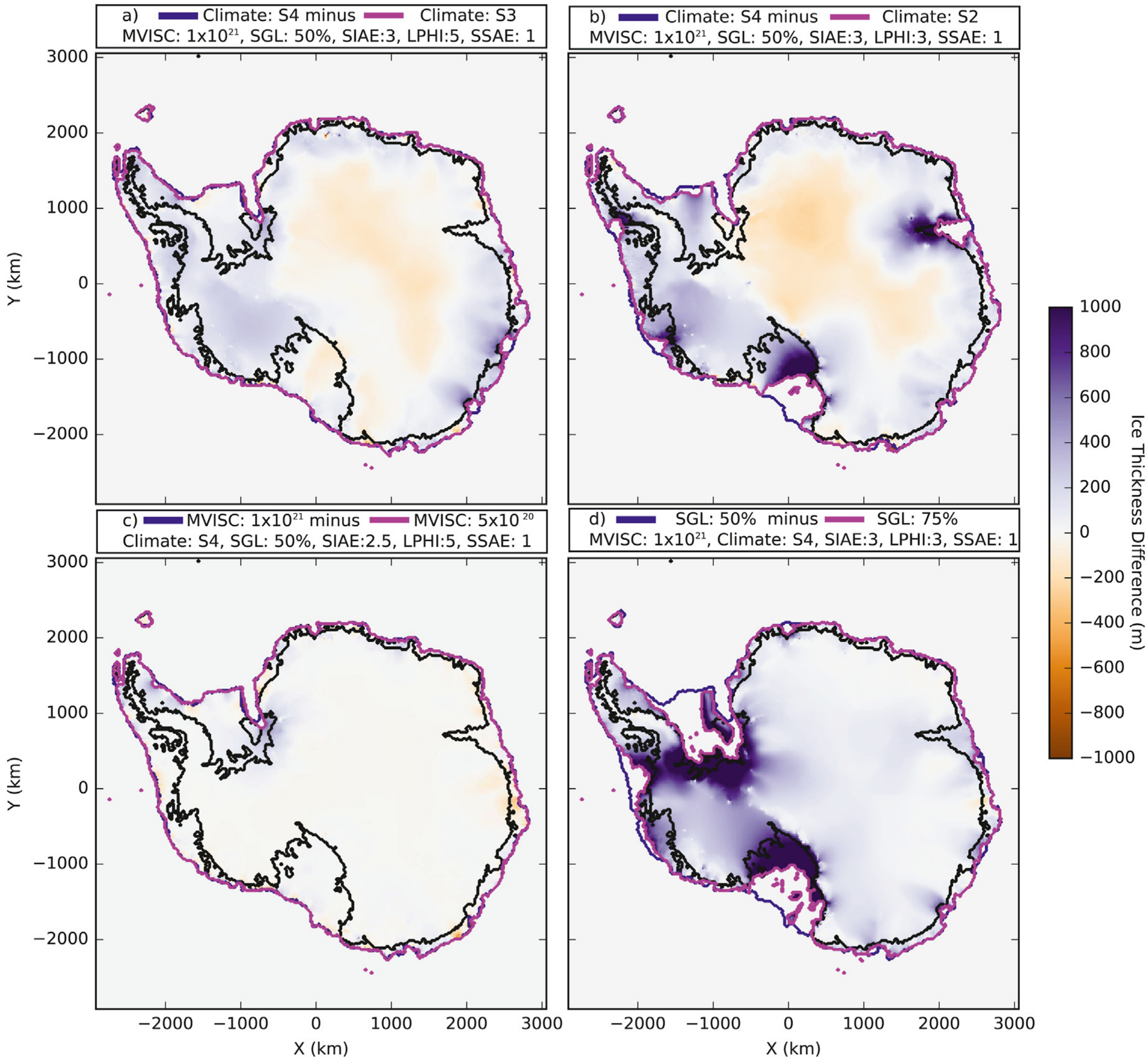

Fig. 6. Effect of key ensemble model parameters. The plots show the difference in grounded ice extent and thickness for the 20 ka timeslice where only one parameter is varied along with the grounding lines for each simulation. Values for non-varied parameters are chosen from high scoring models. (a) Climate S4 (blue) and S3 (magenta) combined with mantle viscosity (MVISC) 1×10^{21} Pa s, SGL 50%, SIAE 3, LPHI 5 and SSAE 1; (b) Climate S4 (blue) and S2 (magenta) combined with mantle viscosity 1×10^{21} Pa s, SGL 50%, SIAE 3, LPHI 3 and SSAE 1; (c) Mantle viscosity of 1×10^{21} Pa s (blue) and 5×10^{20} Pa s (magenta) combined with Climate S4, SGL 50%, SIAE 2.5, LPHI 5 and SSAE 1; (d) SGL of 50% (blue) and 75% (magenta) combined with mantle viscosity 1×10^{21} Pa s, Climate S4, SIAE 3, LPHI 3 and SSAE 1. The present day observed grounding line is plotted in black.

SGL of 50% is for 0 ka, and then it is only marginally better (0.05). We prioritise modelling the LGM advance and therefore select an SGL of 50% for use in Ensemble 2.

5. Ensemble 2

For Ensemble 2 we use climate scenario S4, a mantle viscosity of 1×10^{21} Pa s and an SGL of 50%. These values represent the highest scoring choices amongst the parameters tested in Ensemble 1. In Ensemble 2 we explore in further detail the effect of altering the glaciological parameters SIAE, SSAE and LPHI by running an additional 440 model simulations (Table 6). Parameter ranges and increments are detailed below; they are defined to ensure the inclusion of optimum parameter values.

Table 6
Summary of parameter combinations for Ensemble 2, using the highest scoring options from Ensemble 1 (Climate Scenario S4, Mantle Viscosity 1×10^{21} Pa s and Slipperiness of Grounding Line of 50%). Ensemble 2 explores a wider parameter space and with finer resolution for the glaciological parameters SIAE, SSAE, LPHI than in Ensemble 1.

Ensemble Member	Values	Total Options
Climate Scenarios	S4	1
Mantle Viscosity (Pa s)	1×10^{21}	1
Glaciological Parameters		
SGL	50%	1
SIAE	2, 2.25, 2.5, 2.75, 3, 3.25, 3.5, 3.75, 4, 4.25, 4.5	11
SSAE	0.55, 0.7, 0.85, 1, 1.15, 1.3, 1.45, 1.6	8
LPHI (°)	2, 3, 4, 5, 6	5
Total Models		440

5.1. Ensemble 2 results

Of the 440 Ensemble 2 simulations, 82 passed the sieves applied at the 0 ka time slice (Fig. 7a). The total scores of the passing simulations are in the range 0.57–0.79. The scores for the passing simulations are relatively consistent for the 20 ka and 15 ka timeslices, with a range of 0.62–0.85 and 0.67 to 0.91 respectively. The variability of scores increases for the 10 ka and 5 ka timeslices, with a range of 0.47–0.96 and 0.42 to 0.92 respectively. Scores for the 0 ka timeslice are in the range 0.36–0.57.

The LGM ice volume of the passing simulations (defined as the maximum volume between 22.5 ka and 17.5 ka) varies from 5 to 16 m SLE above present day volume (defined as each simulation's best scoring 0 ka timeslice) (Fig. 7b). The beginning of rapid deglaciation occurs before 15 ka for most passing simulations, with the duration of deglaciation being between 6 kyr and 23 kyr (Fig. 7a). 72 of the simulations have a Holocene minimum below their present-day volume (13 simulations exceed −1 m SLE volume), with the timing of this minimum being between 9.4 and 1.1 ka.

When the 30 top-scoring simulations are investigated further, they have a reasonably narrow range of LGM volumes compared to PD: all but one has a volume excess within the range 10–15 m SLE (Fig. 7b). The duration of deglaciation varies from 8 kyr to 23 kyr

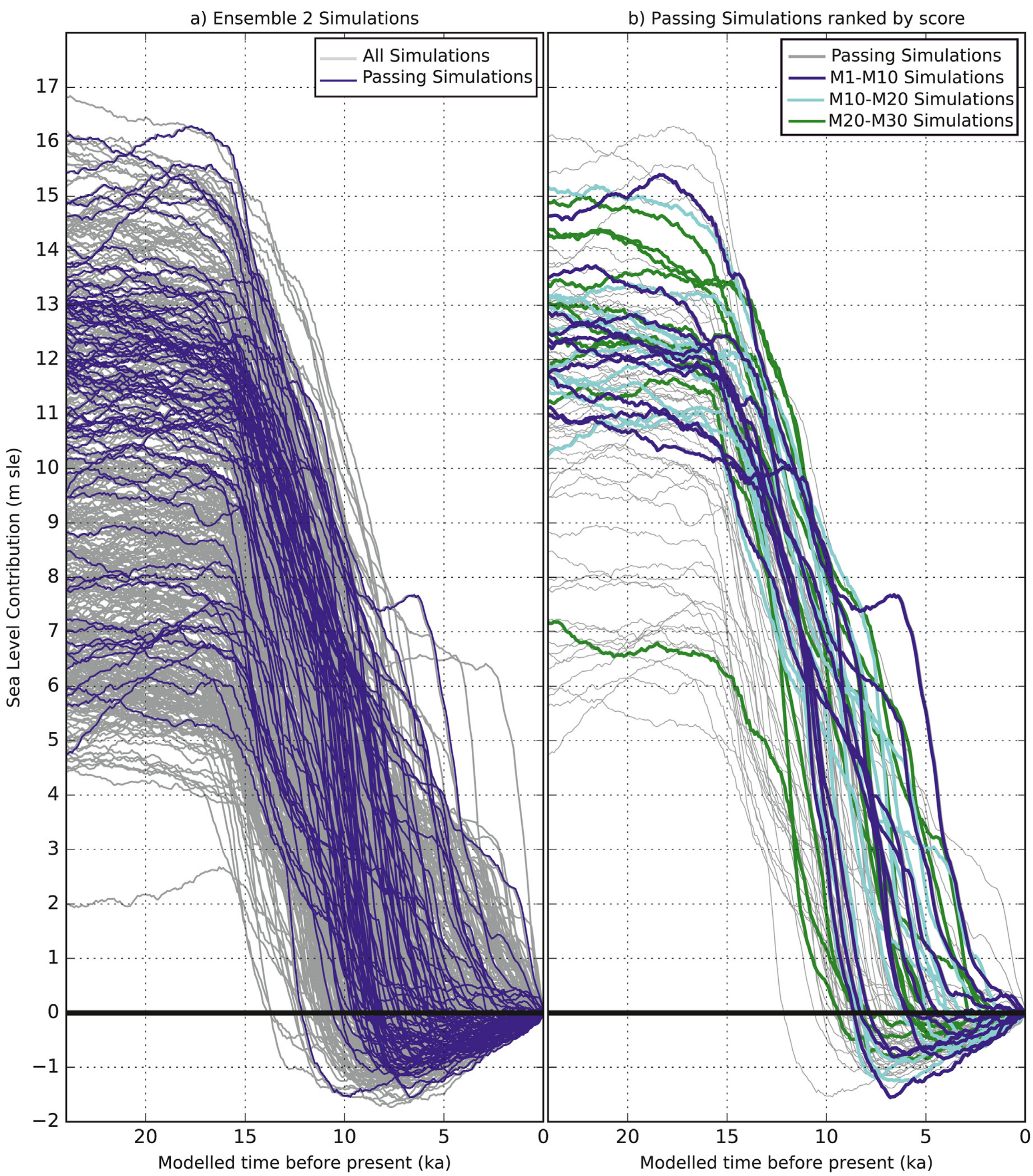

Fig. 7. Sea-level contribution of modelled Antarctic Ice Sheet change through time for Ensemble 2. (a) The 82 (out of 440) simulations which passed the initial sieves are shown in blue, those which failed are in grey. (b) Passing simulations ranked by score: 1–10 in blue, 11–20 in cyan, and 21–30 in green, with the remainder in grey.

and 24 of the top 30 show Holocene volume minima (4 simulations exceed −1 m SLE volume), with the timing of this minimum being between 7.2 and 1.7 ka (Fig. 7b).

5.2. Individual parameters

We sampled three glaciological parameters, the shallow ice approximation enhancement factor (SIAE), the shallow shelf approximation enhancement factor (SSAE), and lower angle in the till parameterisation (LPHI), to investigate how they affect the score or characteristics of deglacial behaviour (Table 7) such as LGM timing (time of greatest volume between 22.5 ka and 17.5 ka), (Fig. 8), LGM volume difference (difference between modelled volume at the LGM and the present day), deglaciation duration (difference between LGM timestep and the timestep when the simulation first reaches its present day volume), Holocene minimum time (timeslice at which volume is lowest) and the Holocene minimum volume (difference between volume at the Holocene minimum time and present day).

The SIAE was varied between 2 and 4.5 using an increment of 0.25. There was no clear trend in score amongst all simulations, but the scoring of the passing simulations indicate that values between 2.5 and 4.5 provide the highest scoring deglacial histories (Fig. 8a). Although a value of 4.25 has the highest average score overall (0.77), with only three passing members we do not suggest it is the best value for the SIAE. The LGM volume difference showed a slight decrease with increasing SIAE for all simulations, which is expected because an increase in SIAE enhances the rate of deformation within the ice which is the primary form of flow in the interior of the ice sheet. The passing simulations had higher average total scores in general compared with all simulations. It is also notable that the passing simulations favour slightly higher LGM ice volumes, by 1–2 m SLE (Fig. 8b).

The SSAE was varied between 0.55 and 1.6 using an increment of

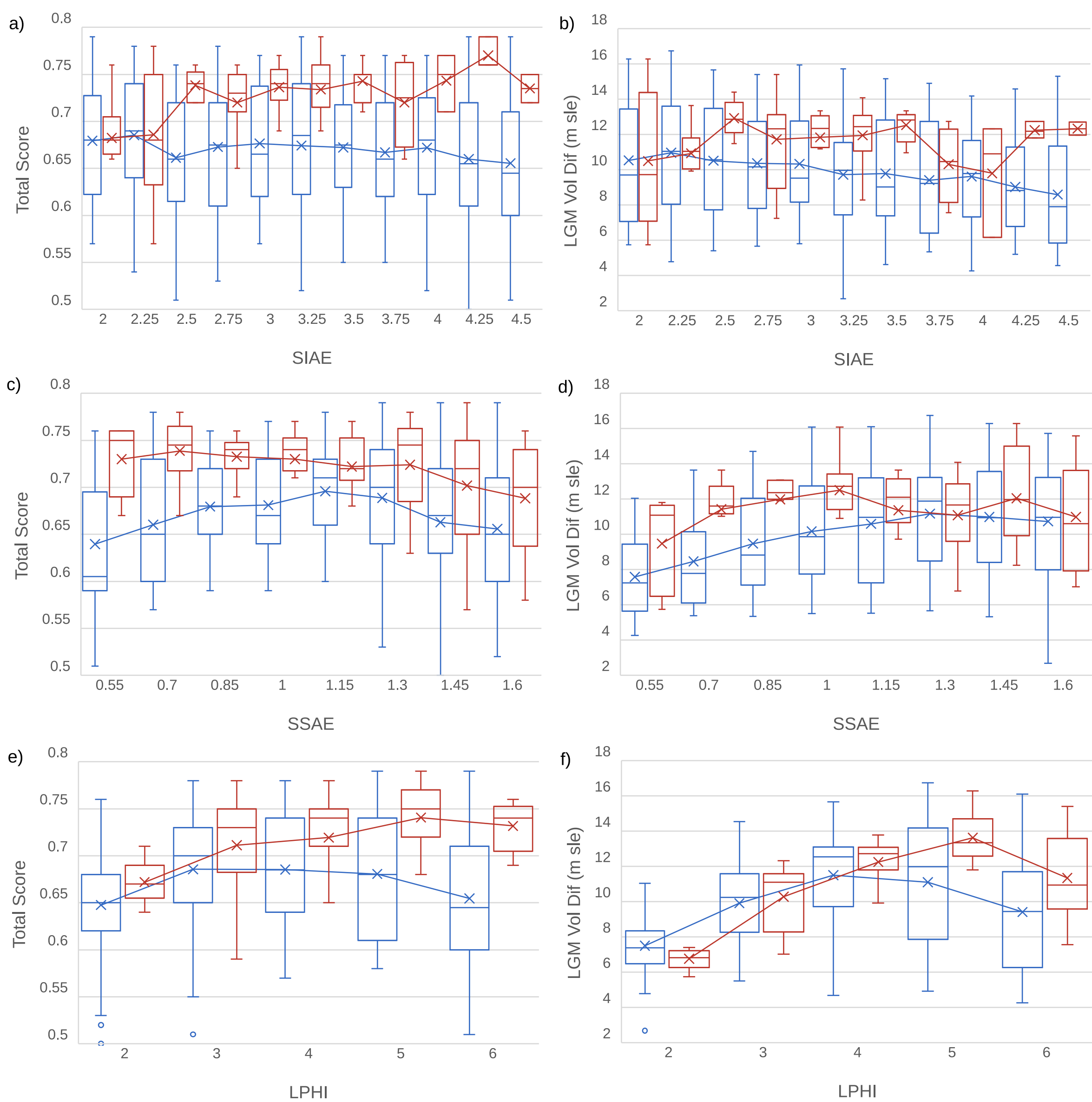

Fig. 8. Box and Whisker plots showing the distribution of total score values (a, c, e) and LGM Volume Difference (Vol Dif) (b, d, f) for a range of values of the glaciological parameters SIAE, SSAE, and LPHI. Excess LGM volume is calculated relative to the modelled PD ice volume in each case. Blue boxes represent all models from Ensemble 2 while red boxes represent just the passing models. Each plot has a line plot joining the median values.

0.15. There is a peak in average score amongst all simulations at 1.15 (Fig. 8c) but the same is not true for the passing simulations. The average score of passing simulations is slightly higher for low values of the SSAE, but SSAE values > 1.15 show a larger range of scores, including higher scoring simulations overall. The LGM volume difference in passing simulations increases from 9.47 m SLE to 12.51 m SLE with increasing SSAE values of 0.55–1, it then plateaus with SSAE values of 1.15–1.45 before slightly decreasing (Fig. 8d). This trend is also seen - albeit less strongly - amongst all passing simulations. The values on the edge of the parameter space have the largest range of possible LGM volumes. The summary deglacial characteristics (Table 7) show that as the SSAE increases, the timing of the LGM shifts to later in the simulation. We speculate that this is because increasing the SSAE increases the rate of flow within ice streams, which enables grounding lines to stay advanced for longer before retreating. However, for higher SSAE values deglaciation tends to be more rapid when it does occur (Table 7) because the interior of the ice sheet has been thinned by rapid ice stream flow during the glacial period.

The LPHI was varied between an angle of 2 and 6° using an increment of 1°. For the full suite of simulations, highest average scores are achieved for LPHI values between 3 and 5° (Fig. 8e). Average scores for passing simulations increase up to till angle of 5°, but are lower for a till angle of 6°. The LGM volume difference increases with increasing LPHI, up to 5°, before decreasing at the upper edge of our parameter space. This trend is more prominent in passing simulations (Fig. 8f). Of the three parameters the LPHI shows the most control over the summary deglacial characteristics (Table 7): an increase in LPHI moves the LGM later, increases the LGM volume difference, increases the deglaciation duration, and shifts the Holocene minima to a later and smaller magnitude volume difference. The LPHI represents the strength of bed resistance. A lower LPHI gives a weaker bed and will lead to faster-flowing and more extensive ice streams, as well as reduced lateral stress at the boundaries of ice shelves. An increase in LPHI will lead to a decrease in flow from the interior of the ice sheet to the coast, which naturally leads to an increase in volume of the LGM ice sheet.

There is a balance within the ensemble between the LPHI, SIAE and SSAE. For example, increasing LPHI reduces the flow from the interior of the ice sheet to the coast, which can be countered by increasing the SIAE which enhances the rate of ice deformation. Similarly, a higher LPHI leads to a reduction in the extent of ice streams, as well as increased lateral stress at the margins of ice shelves, which might be countered by increasing the SSAE to enhance the flow rate of ice streams and ice shelves.

6. Investigation of the top 10 scoring deglacial simulations

6.1. Results

We investigate the top 10 scoring simulations from Ensemble 2, which we label in score order from M1 (highest total score of all passing simulations) through M10 (10th highest total score) (Tables 8 and 9). Within the top 10 simulations the SIAE values range from 2.25 to 4.25, the SSAE from 0.70 to 1.45, and the LPHI from 3 to 5. The LGM volume difference for our top 10 scoring simulations ranges from 10.90 to 14.08 m SLE with varying deglaciation behaviours (Fig. 9a and b). All simulations have a rapid deglaciation that initiates around 15 ka, but prior to this there are three distinct model behaviours (Fig. 9a); a stable ice volume with a slight increase in volume prior to deglaciation (M2,4,5,6,8), a slight but steady volume loss (M3,7,10), or an increasingly rapid volume loss (M1,9). The change in volume during this period is not associated with major changes in grounded area (Fig. 9b) which would be consistent with climatically-driven volume variation rather than dynamic changes.

From 15 ka there are two styles of deglaciation, which have no correlation with the previous groupings. The first is characterised

Table 7
The average statistics from the simulations in Ensemble 2 which passed the sieves. Each of the 82 passing simulations is reported under each of the three glaciological parameters. The average final score is the mean of the final score of passing simulations. See Table 5 for definitions.

Values	No. of Passing Models	Average Final Score	LGM timestep before PD (ka)	Mean LGM Volume difference to PD (m SLE)	Mean Deglaciation Duration (kyr)	Mean Holocene Minimum timestep before PD (ka)	Mean Holocene Minimum Volume difference to PD (m SLE)
SIAE							
2	13	0.68	19.83	10.5	10.72	5.92	−0.83
2.25	12	0.69	19.68	10.93	12.78	5.15	−0.64
2.5	6	0.74	21.22	12.92	15.97	3.6	−0.56
2.75	11	0.72	19.08	11.73	12.91	3.65	−0.48
3	8	0.74	20.79	11.84	15.28	3.8	−0.56
3.25	13	0.73	20	11.95	13.19	4.96	−0.77
3.5	7	0.74	20.04	12.53	15.94	3	−0.37
3.75	4	0.72	20.28	10.31	15.73	3.08	−0.56
4	3	0.75	19.63	9.8	17.1	1.6	−0.21
4.25	3	0.77	20.43	12.25	15.17	3.43	−0.5
4.5	2	0.74	18.05	12.33	13.95	3	−0.7
SSAE							
0.55	5	0.73	21.4	9.47	16.08	3.22	−0.63
0.7	8	0.74	21.84	11.43	15.88	3.39	−0.59
0.85	8	0.73	21.1	11.99	16.61	3.08	−0.49
1	14	0.73	21.3	12.51	15.82	4.19	−0.58
1.15	14	0.72	19.19	11.36	12.44	4.64	−0.66
1.3	10	0.72	19.23	11.09	11.51	5.15	−0.83
1.45	11	0.70	18.2	12.04	11.65	4.43	−0.59
1.6	12	0.69	18.77	10.98	12.03	4.87	−0.5
LHI							
2	5	0.67	20.08	6.76	9.38	7.54	−1.19
3	26	0.71	20.37	10.29	12.89	5.06	−0.72
4	28	0.72	20.09	12.15	14.44	4.28	−0.55
5	16	0.74	19.3	13.25	14.33	3.11	−0.45
6	7	0.73	19.14	12.05	14.83	2.24	−0.42

Table 8
The Top 10 scoring simulations from Ensemble 1 and 2 along with our scoring of four published deglacial models. Only Albrecht et al. (2020b) is scored for 0ka as it was the only deglacial history to dynamically model the 0ka timestep. The thinning rate value refers to the number of geologically-derived thinning rates that are matched (within 2-sigma) by the modelled thinning rates at those locations.

Ensemble Parameters							Thinning Rates	Scoring by Timeslice				Scoring Summary		
Simulation	Climate	Mantle viscosity (Pa s)	SGL	SIAE	LPHI (°)	SSAE	Score (out of 25)	20ka	15ka	10ka	5ka	Paleo	0ka	Total Score
M1	S4	1×10^{21}	50%	3.25	5	1.45	13	0.83	0.86	0.86	0.86	0.85	0.55	0.79
M2	S4	1×10^{21}	50%	4.25	5	1.45	12	0.8	0.84	0.96	0.85	0.86	0.5	0.79
M3	S4	1×10^{21}	50%	2.25	3	0.7	13	0.81	0.88	0.86	0.83	0.85	0.52	0.78
M4	S3	1×10^{21}	50%	3	5	1	20	0.8	0.85	0.84	0.89	0.84	0.52	0.78
M5	S4	1×10^{21}	50%	2.25	4	1.3	11	0.8	0.87	0.84	0.85	0.84	0.53	0.78
M6	S4	1×10^{21}	50%	4	4	1	17	0.8	0.86	0.86	0.84	0.84	0.51	0.77
M7	S4	1×10^{21}	50%	3.25	5	1.3	22	0.82	0.85	0.81	0.84	0.83	0.53	0.77
M8	S4	1×10^{21}	50%	3.5	5	1.15	19	0.79	0.89	0.81	0.84	0.83	0.52	0.77
M9	S4	1×10^{21}	50%	3.75	3	0.7	14	0.8	0.88	0.84	0.88	0.85	0.44	0.77
M10	S4	1×10^{21}	50%	3	5	1	19	0.8	0.86	0.81	0.88	0.83	0.49	0.77
5G (Peltier, 2004)							19	0.31	0.59	0.69	0.65	0.56	n/a	n/a
6G (Argus et al., 2014)							15	0.61	0.74	0.64	0.71	0.68	n/a	n/a
W12 (Whitehouse et al., 2012a)							10	0.84	0.79	0.8	0.65	0.77	n/a	n/a
A20B (Albrecht et al., 2020b)							14	0.92	0.84	0.58	0.83	0.79	0.66	0.77

Table 9
Summary of deglacial behaviour and volume change of the top 10 scoring simulations.

Simulation	LGM timestep before PD (ka)	LGM Volume difference to PD (m SLE)	Deglaciation Duration (kyr)	Holocene Minimum timestep before PD (ka)	Holocene Minimum Volume difference to PD (m SLE)	Absolute difference to PD volume (m SLE)
M1	22.7	12.81	14.3	4.8	−0.47	0.12
M2	16.8	11.81	8.5	5.3	−0.7	−0.22
M3	22.2	11.63	13.2	5.4	−0.97	1.67
M4	15.7	11.9	9.8	1.7	−0.34	2.81
M5	17.4	10.9	9.1	6.8	−0.83	2.48
M6	18.2	12.32	15.4	2.1	−0.32	−0.08
M7	21.8	14.08	17.5	3	−0.62	−0.14
M8	19	13.35	13.2	3.8	−0.6	0.89
M9	21.5	11.03	14.7	4.8	−1.12	−0.93
M10	23.4	13.34	21	1.3	−0.1	2.03

by rapid deglaciation to an ice volume below that of present day by 7.5 ka (M1,2,3,5), while the second has a slower deglaciation period followed by a tail of different behaviour as the simulations approach present day volume (M4,6,7,8,9,10). Grounded area change follows a similar range of trajectories (Fig. 9b), although the differentiation between simulations is less clear, especially as the grounded area approaches 100% of the present day timeslice. The exceptions are M3, M4 and M9 which rapidly retreat to a grounded area smaller than present during the early Holocene, reflecting a period of rapid dynamic retreat.

Our top 10 results demonstrate the balance between LPHI and the two enhancement factors (SIAE and SSAE, Table 8): in other words the balance between strength of the bed and strength of the ice. For example, simulations M1 and M2, which have an LPHI of 5, also have relatively high SIAE (3.25,4.25) and SSAE (1.45,1.45) values, compared with M3 and M9, which have an LPHI of 3 and lower SIAE (2.25,3.75) and SSAE (0.7,0.7) values. This highlights the non-uniqueness inherent in ice sheet modelling and the need to consider more than one best-fit result, and it further supports our ensemble approach.

6.2. Comparisons to existing models

To test our scoring method beyond our own ensemble we additionally apply it to four existing deglacial reconstructions; ICE-5G (Peltier, 2004), ICE-6G_C (Argus et al., 2014), W12 (Whitehouse et al., 2012a), and the top ensemble member (A20B) from Albrecht et al. (2020b). This allows us to score the relative performance of the simulations within our ensemble against output from previously published models, and to see which of our ensemble simulations, if any, score better in our scheme than previous deglacial reconstructions (Table 8). ICE-5G was constructed using a combination of paleo ice sheet observations and far-field sea-level data. ICE-6G_C represents an update to ICE-5G; comparing the two ice histories should allow us to determine whether our scoring method can identify any improvement between iterations of the ice history. The W12 model was developed using the Glimmer ice model, with fixed grounding line positions defined at 20 ka, 15 ka, 10 ka, 5 ka and 0 ka. A20B is a numerical simulation produced using the PISM model, it was originally scored using the AntICEdat dataset of compiled geological observations (Briggs and Tarasov, 2013; Albrecht et al., 2020b).

Scoring these four deglacial histories is important because it not only provides a direct comparison for our new deglacial reconstructions but also because the models have been constructed using different approaches and understanding their relative performance against constraint data may provide insight into the utility of these approaches. Moreover, the pre-existing ice histories differ in terms of their total LGM ice volume and style of deglaciation. In terms of excess ice volume at the LGM, ICE-5G (17.5 m SLE) and ICE-6G_C (13.6 m SLE) (Argus et al., 2014) have more than W12 (9 ± 1.5 m SLE) or A20B (9.4 ± 4.1 m SLE).

The scores in Table 8 show that three of the four previously published deglacial models score lower for almost all timeslices than our top 10 scoring simulations. The exception is W12, which scores higher (0.84) for the 20ka timeslice than our top 10 (highest score 0.83). W12 also performs similarly to our top 10 for the 10ka timeslice, where it scores only fractionally lower (0.80) than the three lowest scoring of our top 10, which score 0.81. The fourth published model, A20B, has an overall score (0.77) close to our top

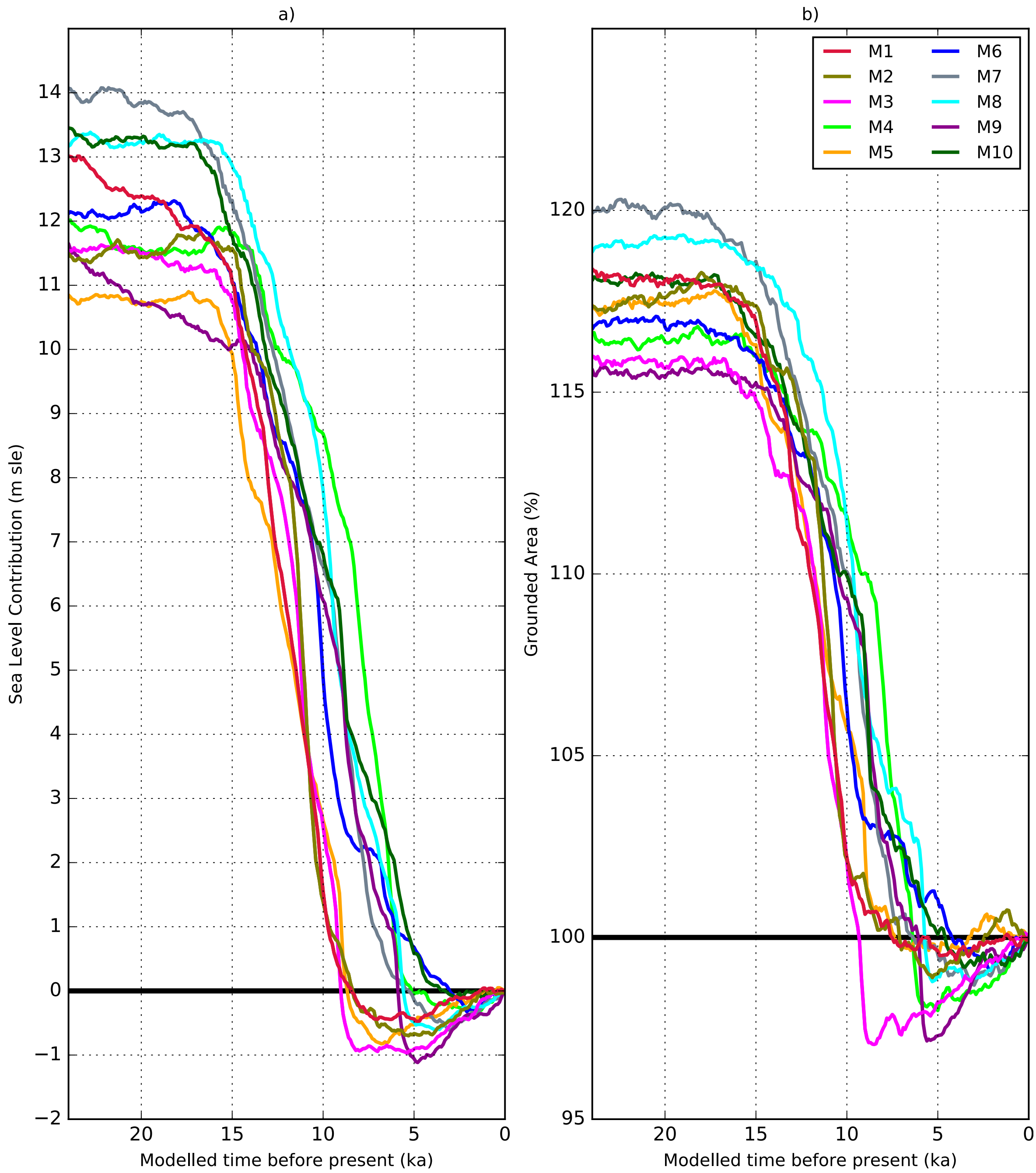

Fig. 9. Evolution of the top 10 scoring simulations from both Ensembles shown in terms of (a) sea level contribution (m SLE) and (b) grounded area (normalised to best scoring present day time step). Details of ensemble parameters for M1-M10 are in Table 8, and a summary of volumes and deglacial timing characteristics are in Table 9. Colours correspond to Figs. 10 and 11.

10 (0.77–0.79). This high scoring of A20B is driven by relatively higher scores for the 20 ka and 0 ka timeslices compared to our top 10. A20B has comparable performance to our top 10 for the 15 ka, and 5 ka timeslices (Table 8). Interestingly, the score for the A20B 10 ka timeslice is notably low (0.58), and indeed lower than any of the previously published models or our top 10.

7. Discussion

In this section we discuss the characteristics of the 10 top-scoring simulations, and specifically what inferences can be made from them about patterns of Antarctic deglaciation. Five key themes emerge; 1) LGM ice sheet volume (sea level contribution); 2) regional behaviour of the ice sheet, specifically in the Ross Sea sector; 3) retreat behind present margins in the Late Holocene; 4) readvance mechanisms; 5) the use of geologic data and data-model comparisons. We discuss these themes in turn.

7.1. Ice sheet volume through time

Our modelled ice volume excess at the LGM (range of 10 top-scoring simulations equals 10.9–14.08 m SLE; Table 9; Fig. 9a) is slightly higher than, but overlaps with, the value of 9.9 ± 1.7 m SLE determined from estimates compiled since 2010. It also overlaps with the range of 7.5–13.6 m SLE derived from three GIA studies (Simms et al., 2019). In terms of how the previously published models score during deglaciation, both W12 and A20B score higher than the top 10 simulations in our ensemble for the 20 ka timeslice (Table 8). This higher match may suggest that the lower excess volumes at LGM of W12 and A20B are preferred by the geological data, which is supported by the progressively lower scores for ICE-6G_C and ICE-5G for the 20 ka timeslice. The top 10 simulations in our ensemble all score higher for each of the 15 ka, 10 ka, and 5 ka paleo time-slices than any of the four previously published deglacial models. However, A20B scores more highly for the 0 ka time-slice than any of our top 10.

Fig. 10 shows the differences between the 10 top-scoring simulations at their 20 ka configuration. The 20 ka grounding line positions are shown in Fig. 10a, and demonstrate that there is little variation in positions between the best-scoring simulations except in the Ross Sea and Prydz Bay. Here, simulations with smaller grounded area and volume (Fig. 9) have larger embayments in the central Ross Sea and central Prydz Bay. More broadly, most of the volume differences occur due to differences in ice elevation in the south-eastern Weddell Sea sector, Ross Sea sector, and Amery-Lambert glacial system (Fig. 10b–d). These volume differences at 20 ka occur where there were former embayments in the grounding line in each of the Weddell, Ross and Prydz Bay systems. The variability in modelled grounding line positions in these high scoring simulations probably reflects a relative lack of marine geological constraints in the central parts of the embayments and the fact that geological evidence of ice thickness at coastal nunataks is too distant to have significant constraining power on the grounding line, particularly when it is at or near maximum extent.

Notably all of the top-scoring simulations show little difference in the extent of the grounding line on the continental shelf around the Antarctic Peninsula and Bellingshausen - Amundsen Sea sectors, with all high scoring simulations having grounded ice extending to the shelf edge. There are some minor differences in extent on the East Antarctic shelf with some of the smaller simulations having embayments in Wilkes Land, which is also reflected by thinner ice directly inland.

The timing and nature of deglaciation shows some variation in our top-scoring simulations. Although most of the top 10 simulations keep a reasonably constant grounded area from 25 ka to 17 ka (Fig. 9b) it is noticeable that ice sheet volume shows more variable behaviour. Most simulations have fairly constant volume but some (e.g. M1, M3, M9) show a steady, relatively slow decline prior to rapid deglaciation (Fig. 9a). This suggests that in these simulations there may have been substantial thinning prior to grounding line

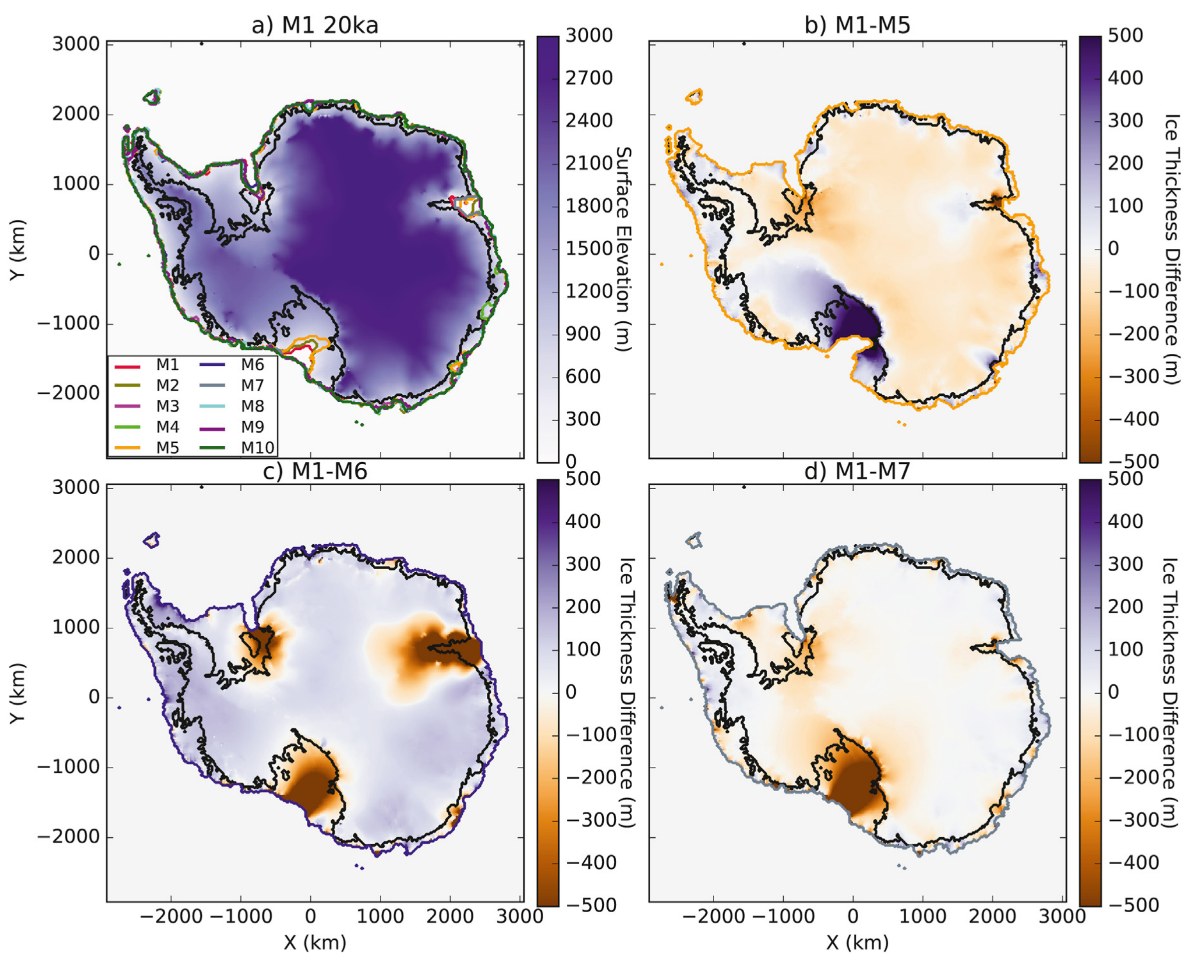

Fig. 10. Differences in modelled ice sheet configuration at 20 ka. Line colours correspond to Fig. 9 a) Modelled M1 surface elevation at 20 ka and grounding lines for the top 10 scoring simulations; b) 20 ka grounding line for M5 and ice thickness difference between M1 and M5. M5 is chosen as an example of a model with a relatively small LGM volume (Fig. 9) but with a similar deglacial trajectory to the majority of the top 10 simulations; c) Ice thickness of M1-M6 and M6 grounding line at 20 ka. M6 is chosen as a simulation with similar LGM volume to M1 but which deglaciates more slowly; d) M1-M7. M7 is the top 10 simulation with the largest LGM volume, and it deglaciates relatively late compared to other top scoring simulations. In each case the volume differences - whether smaller or larger than M1 - are dominantly focussed on the SE Weddell Sea, Ross Sea and the Prydz Bay/ Amery Ice shelf region.

retreat. The timing of the onset of more rapid deglaciation (i.e. where gradients steepen in Fig. 9a) varies within a fairly small time interval from 17.5 ka (M6, M7) to 15 ka (M2, M4, M9).

All of our 10 top-scoring simulations have major deglaciation occurring by 15 ka, consistent with a range of marine geological evidence for the timing of ice stream retreat (Livingstone et al., 2012; Bentley et al., 2014). Livingstone et al. (2012) show that the retreat behaviour of individual ice stream catchments varied markedly depending on drainage-basin size, bathymetry, bed roughness and ice-stream geometry, and we emphasise that Fig. 11 shows the behaviour in aggregate, which will likely mask huge variations in retreat timing and style. However it is notable that very little terrestrial evidence exists for such early rapid deglaciation with cosmogenic exposure ages evidencing a pulse of rapid thinning in the early-mid Holocene (Johnson et al., 2014; Jones et al., 2015; Hein et al., 2016; Small et al., 2019). Our best scoring simulations suggest that the early lateral retreat of ice streams, as documented by geological evidence, was likely accompanied by a significant reduction in ice sheet volume with implications for the source areas of Antarctic contributions to global sea level change at this time.

We score all models against two grounding line scenarios which differ in the Weddell Sea (Hillenbrand et al., 2014) but point out that these scenarios are treated equally in the scoring scheme. Our top 10 scoring simulations show matches to one or other of these scenarios, but we also note some key differences when compared to our simulated LGM configurations. Scenario A has two embayments, one in the Filchner ice shelf and one in the Ronne ice shelf, located either side of a region of ice sheet advance to the continental shelf (Hillenbrand et al., 2014). Scenario B assumes ice sheet advance to the continental shelf across the whole embayment (Bentley et al., 2014). All of our Top 10 scoring simulations (Fig. 10a), are simulations that show a large embayment in the Filchner Ice Shelf, but we do not reproduce an embayment on the Ronne ice shelf side.

Fig. 11 shows the position of the grounding line at various times for some top-scoring simulations. Some simulations appear to retreat very early. For example, M2 has retreated in both the Weddell and Ross Sea by 10 ka. This is initially surprising, however it can be explained by the fact that both the minimum and

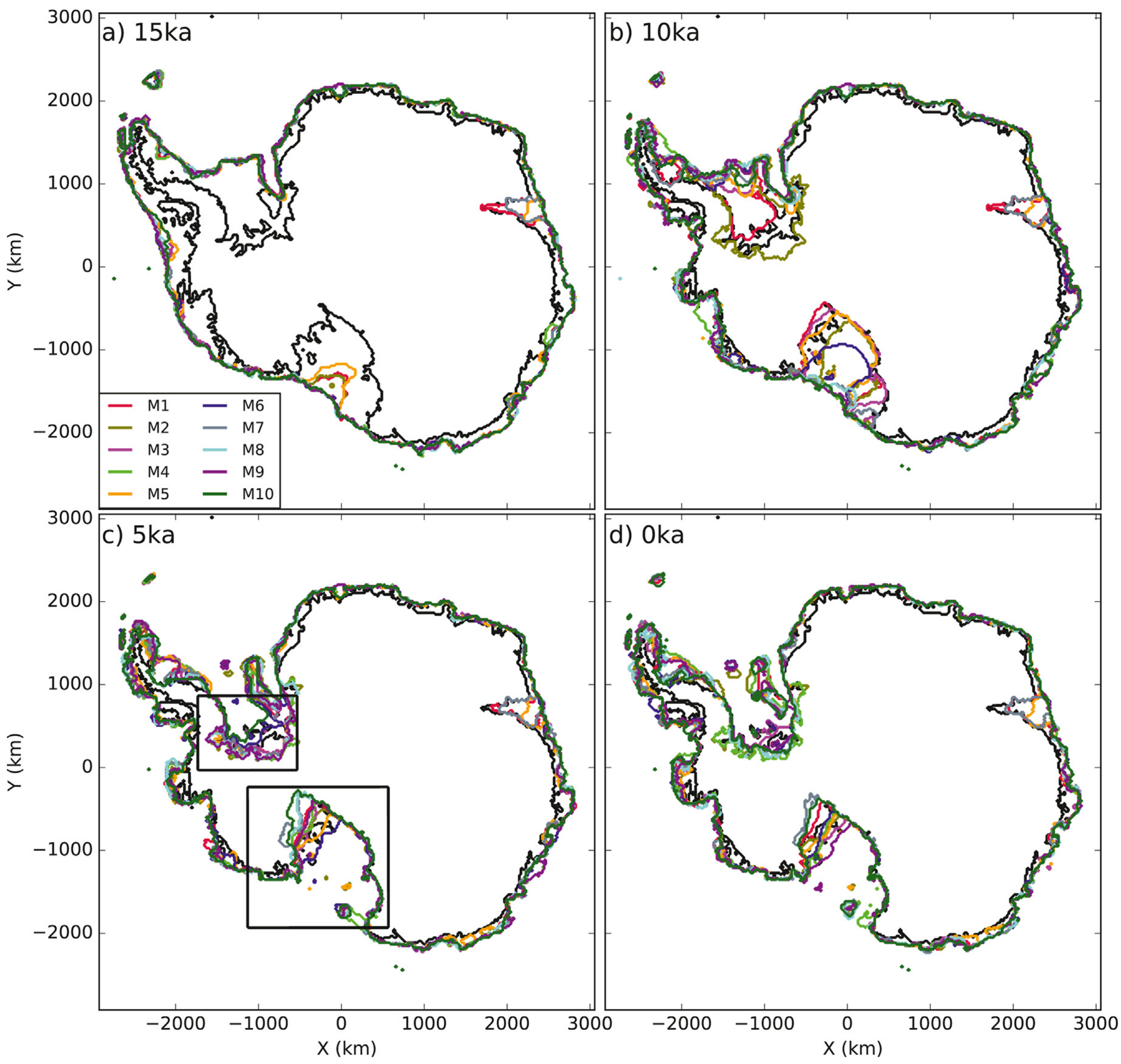

Fig. 11. The grounding lines for the top 10 scoring simulations along with the present day observed grounding line (Bedmap2, Black) are shown for (a) 15ka, (b) 10ka, (c) 5ka and (d) 0ka. The boxed outlines on (c) show the regions displayed in Figs. 11 and 12.

maximum RAISED scenarios for the Weddell Sea sector are treated equally in the scoring scheme. This allows more retreated configurations in the Weddell Sea to score highly against the minimum scenario influencing the overall score of this simulation. Interestingly, we note that simulations M3 and M5 show significantly earlier retreat in the Ross Sea than in the Weddell Sea, so for example the Ross Sea grounding lines retreat to close to present values whilst the Weddell Sea grounding lines are still in intermediate positions (Fig. 11b and c).

7.2. Holocene retreat behind present grounding line

A notable feature of a large number of the 82 passing model simulations in Ensemble 2 and all of the top-scoring 10 simulations is that they show a minimum in ice sheet volume prior to the present day (Fig. 9). For most of these simulations there is a corresponding minimum in grounded area, implying that the grounding line is modelled to have retreated behind its present position in some sectors of the ice sheet. The existence of a smaller-than-present ice sheet (or 'overshoot') configuration in the mid-to late Holocene has been suggested in both the Weddell Sea (Bradley et al., 2015; Bentley et al., 2017; Whitehouse et al., 2017; Siegert et al., 2019) and Ross Sea (Kingslake et al., 2018; Venturelli et al., 2020; Neuhaus et al., 2021). The inference of retreated positions relies on a range of datasets including marine geological observations of former grounding lines, glaciological observations, GPS-measured subsidence, and radiocarbon inventories in sediments located behind the present grounding line. Possible mechanisms for this retreat and subsequent re-advance, including GIA-induced re-grounding of ice shelves (Matsuoka et al., 2015; Bradley et al., 2015; Kingslake et al., 2018) or climatic controls (Lowry et al., 2019; Neuhaus et al., 2021).

Fig. 11c shows that by the mid-Holocene many of the top-scoring simulations predict retreat behind the present grounding line position in the Ross Sea and south-eastern Weddell Sea. Figs. 9 and 11 together show the influence of the timing of grounding line retreat on the volume evolution of the modelled ice sheet. For example, simulations M8 and M10 predict an advanced position of the grounding line in the Weddell Sea and Ross Sea until well into the Holocene (Fig. 11b and c) and this is reflected in slower and later retreat and ice volume and area decline (Fig. 9). Other simulations predict an earlier retreat, especially in the Ross and Weddell Sea embayments (Fig. 11), and this is reflected in earlier volume decline. Two of the simulations (M3 and M5) reach their smaller-than-present volume minima at or before 7 ka but the majority of smaller-than-present minimum configurations are reached after 7 ka. This is consistent with the emerging evidence from radiocarbon inventories in sediments of the Ross Sea which argue against model predictions of early Holocene retreat to smaller-than-present configurations (Kingslake et al., 2018) and supports reconstructions that place the timing in the mid-Holocene (Venturelli et al., 2020). A mid-Holocene minima is also more consistent with exposure age dating of outlet glacier thinning in the Transantarctic Mountains (Spector et al., 2017).

More detailed analysis of the readvance positions of some of the top 10 simulations in the Ross and Weddell Sea regions are shown in Fig. 12 (Ross Sea) and Fig. 13 (Weddell Sea). The pattern of grounding line change in the Ross Sea shows that from the mid to Late Holocene up until the present-day there was advance at a similar rate across the whole of the Siple Coast region (Fig. 12), although not all high-scoring simulations precisely simulate the present-day grounding line (Fig. 12b).

The magnitude of Holocene 'overshoot' retreat on ice sheet volume ranges from −0.1 to −1.1 m SLE (Fig. 9, Table 9), with most in the range −0.4 to −1.0 m. This has potential implications for studies that attempt to balance the global sea level budget: rather than a continuous contribution to sea-level rise up to present, it is possible that re-growth of the Antarctic ice sheet was offsetting sea-level rise from elsewhere during the mid to late Holocene.

In Ensemble 1 there was a correlation between the volume of the Holocene minimum and mantle viscosity (Table 5), with higher viscosity simulations predicting the smallest Holocene minima and lower viscosity simulations predicting minimal retreat behind present, likely due to the stabilising effect of rapid rebound (Gomez et al., 2015). Our results support the idea that mantle viscosity, and hence the rate of solid Earth rebound during deglaciation, plays a role in controlling the timing and extent of retreat/readvance. Ice-Earth feedbacks have been shown to be important in low viscosity regions such as the Amundsen Sea Embayment (Kachuck et al., 2020) but more work is needed to understand the role of feedbacks in regions where mantle viscosity is uncertain and may vary laterally, e.g. across the Weddell and Ross Sea regions (Whitehouse et al., 2019).

7.3. Patterns of deglaciation in the Ross Sea

In the Ross Sea, the highest scoring simulations document a range of Holocene behaviour with many of them predicting a central embayment in the grounding line by 10 ka (Fig. 12b). The dimensions of this embayment differ between simulations but in all cases rapid grounding line retreat is predicted between 10 and 8 ka, particularly in the western Ross Sea (Fig. 12a,c). By 8 ka the grounding line is consistently modelled to be close to its current position along the front of the Transantarctic Mountains. In some simulations, continued Holocene retreat is predicted up to 400 km behind the present grounding line (Fig. 12a). For example, in simulation M7 significant inland retreat is predicted along the Mercer Ice Stream (adjacent to the Transantarctic Mountains) by 7–6 ka. This is followed by slow readvance during the late Holocene that does not reach the present-day grounding line (Fig. 12b). We also illustrate the behaviour of M18, and although it was the 18th best scoring simulation, it shows an important type of behaviour. Out of our top 30 this simulation is the one with the greatest Holocene retreat behind present margins but which still readvances to the present day by 0 ka. M18 predicts ~400 km retreat behind present along the whole Siple Coast by 7 ka and subsequent progressive readvance reaches the present day grounding line by 10 ka (Fig. 12c and d).

There is ongoing debate as to whether a 'swinging gate' or a 'saloon door' best describes the pattern of ice sheet retreat in the Ross Sea (Halberstadt et al., 2016). The swinging gate model proposes a linear grounding line retreat deglaciation, hinged in the eastern Ross Sea and thus showing progressive retreat of the grounding line through much of the mid to late Holocene in the western Ross Sea, along the Transantarctic Mountain front. The saloon door model suggests that deglaciation was more rapid in a large embayment in the central Ross Sea with slower grounding line retreat simultaneously in both eastern and western Ross Sea. Our highest scoring simulations do not discriminate clearly between these two conceptual models: modelled initial retreat supports the suggestion that a central embayment developed in the Ross Sea during the Holocene (Halberstadt et al., 2016; Greenwood et al., 2018) but does not preclude a linear deglaciation in the western Ross Sea. For example Fig. 11a and b and 12a, c show that some of the high scoring simulations show a large central embayment. But the modelled retreat behaviour along the Transantarctic Mountain Front is more complex. Specifically, simulations M7 and M18 show an initial embayment but with rapid retreat of a grounding line perpendicular to the Transantarctic Mountain front of > 1000 km in less than 2 kyr and relatively early in the Holocene

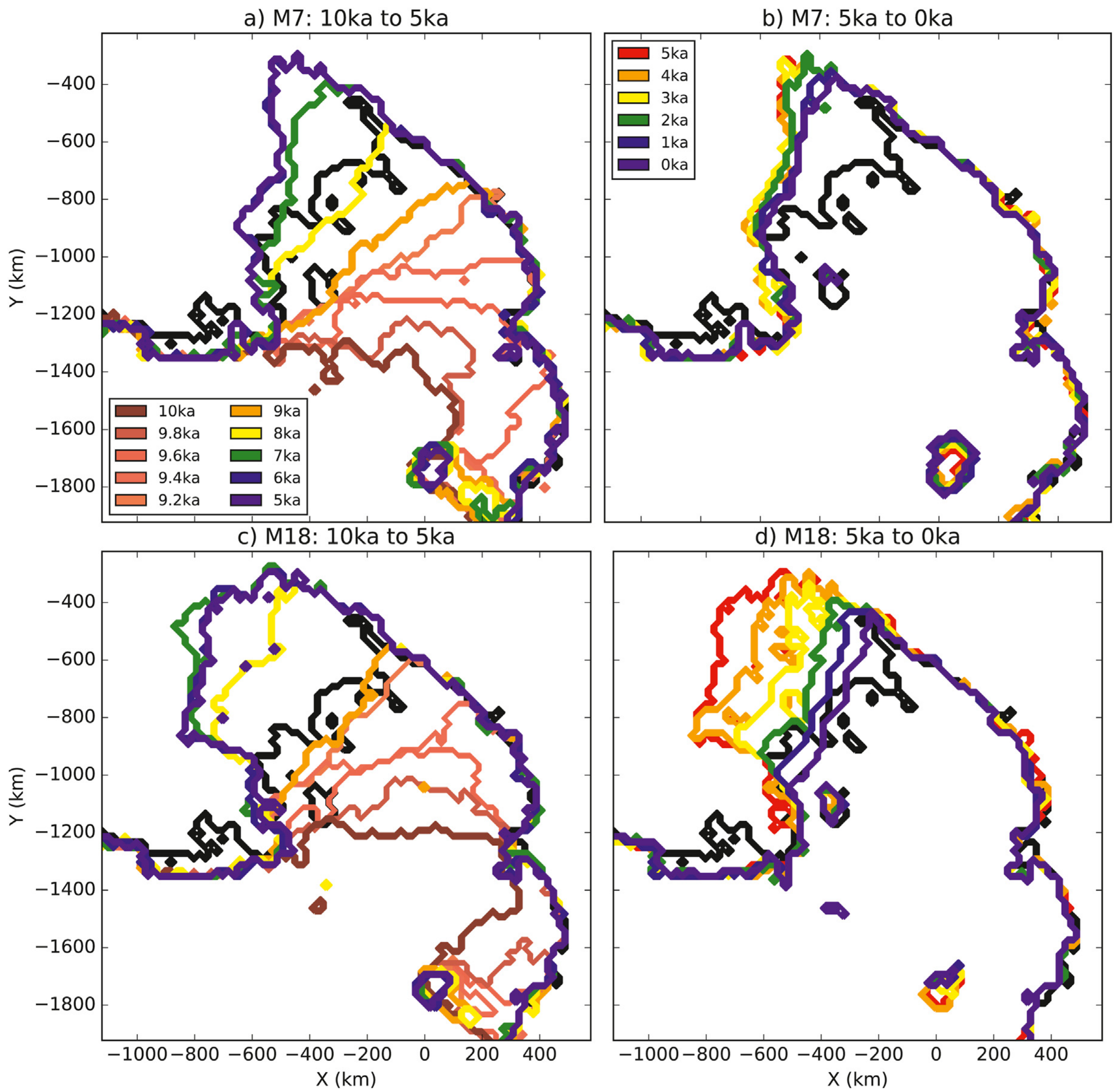

Fig. 12. Holocene retreat in the Ross Sea. Map of the Ross ice shelf region for simulation M7 (a, b) and M18 (c, d) with grounding lines plotted through time. (a, c) 10ka through to 5ka, (b, d) 5ka through to 0ka. The observed grounding line is in black (BEDMAP2). Most modelled grounding lines are shown at 1 ka intervals but between 10 and 9ka we show grounding lines at 200 a intervals in order to display modelled retreat styles. Colour keys in panels a and b also apply to c and d, respectively.

(Fig. 12a). But there are remnants of grounded ice in the western Ross Sea for a few kyr following this retreat. In both cases there is modest retreat (200–400 km) in the eastern Ross Sea during the same interval.

7.4. Readvance mechanisms in the Wedell sea sector

We explore the mechanisms of ice sheet readvance from smaller-than-present configurations in Fig. 13. Fig. 13b shows that a large part of the ice sheet in the southern part of the Weddell Sea embayment - beneath the current-day Filchner-Ronne ice shelf (FRIS) - ungrounds at 6 ka. This un-grounding is rapid and extensive, a 1000 m-deep cavity forms beneath the ice shelf as the grounding line retreats to a position 200 km inland of the present-day grounding line (Fig. 13a). Over the following 3–7 kyr the water depth subsequently shallows at all sites (Fig. 13b). This reflects a combination of slow isostatic rebound and a thickening of the ice shelf, which progressively regrounds (Fig. 13d). The deepening of the ice shelf keel due to thickening occurs at a rate up to three times faster than the rate of the bed uplift (Fig. 13d). We cannot rule out that some of the thickening of the ice shelf is itself driven by re-grounding or an increase in lateral stress elsewhere in the embayment. The location of the first re-grounding is the current Henry Ice Rise, about 3 kyr after the initial un-grounding. Re-grounding then occurs 1–4 kyr later at sites inland of the present-day grounding line with the furthest inland sites grounding before the intermediate site (Fig. 13b). The pattern of grounding is controlled by the bed topography with shallow areas of bathymetry - such as beneath the Henry Ice rise - being the likely sites for re-grounding. This localised grounding and ice rise formation (Fig. 13c) appears to be critical in triggering readvance, and is consistent with the mechanism discussed by Matsuoka et al. (2015) whereby GIA-driven or climatically driven ice thickening causes the ice to re-ground on an uplifting seabed, leading to the formation of

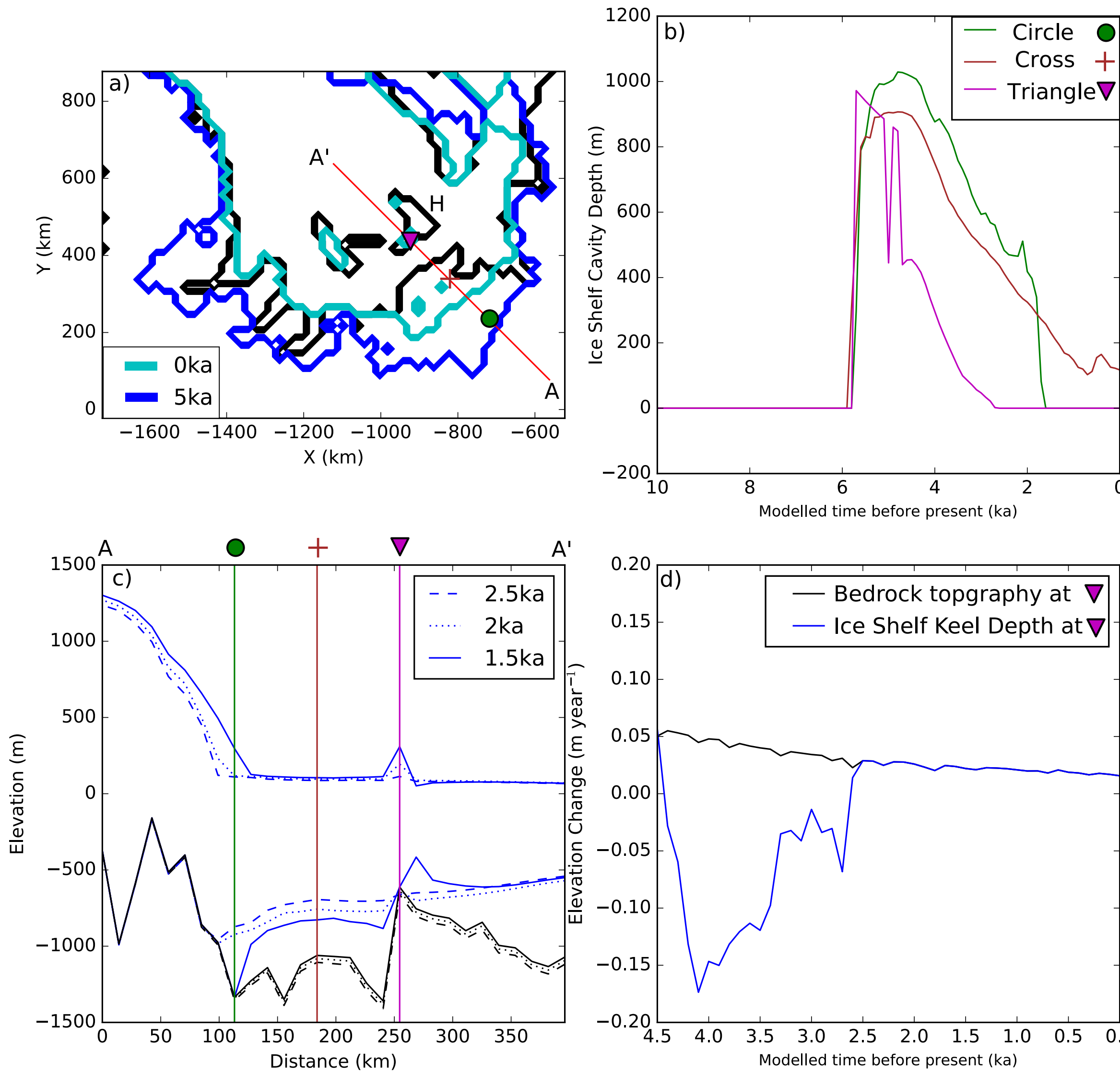

Fig. 13. Readvance mechanisms in the Weddell Sea. (a) A map of the Filchner-Ronne Ice Shelf (FRIS) with the grounding line from simulation M9 at 5ka in blue and at 0ka in cyan (extent of map shown in Fig. 10c). The green circle, brown cross and magenta triangle show the locations of the time series plotted in b, while the red transect indicates the location of the profiles plotted in c. H indicates the location of the Henry Ice Rise; (b) Depth of the water beneath the ice shelf (or open ocean) through time showing when different regions transition from grounded to floating or open water, and then re-ground again. The abrupt cavity changes at the outermost (triangle) site between 6 and 4.5ka are due to minor fluctuations of a calving front over the site; (c) Configuration of the ice sheet and bed just after the time at which re-grounding occurs (c. 2.7 ka) at the magenta triangle in panel a. Top and underside of the ice shelf are shown by blue lines and the bed in black. Vertical lines correspond to colours in panel a. (d) Contribution of bed uplift and ice thickness change to re-grounding, shown for the magenta triangle site in a. The plot shows that the underside of the ice shelf lowers (thickens) at about three times the rate that the bed is uplifting. The cavity closes when the ice shelf grounds at 2.7 ka.

ice rises. The ice rises in the southern Weddell Sea are likely to impart backstresses and consequently trigger ice sheet re-advance (Matsuoka et al., 2015; Kingslake et al., 2018; Siegert et al., 2019).

7.5. Data-model comparison and implications for future field campaigns

We use a comprehensive set of geological data to identify the most realistic reconstructions of Antarctic Ice Sheet change during the last deglaciation but there is significant variability in our top-scoring simulations (Fig. 14). The variability is of interest because it can point to areas where new geological constraints are likely to have greater power to discriminate between simulations. The greatest variation is seen across regions currently covered by ice shelves. This variability is partly related to the difficulty of identifying and dating geological records of past ice extent and thickness in marine-grounded sectors of the ice sheet. Marine records of past grounding line positions are often difficult to access due to the presence of contemporary ice shelves and, by definition, there are rarely any nunataks to record past ice thickness near the centre of the marine embayments - such features are predominantly located near the coast of terrestrial sectors or along the Transantarctic-Peninsula mountain range. It is therefore not surprising that the greatest variability in modelled change is seen in sectors that experienced the most grounding line migration during the last glacial cycle. Although potentially challenging, improving data coverage and quality in these sectors is desirable given the wide range of factors that control their ice dynamics.

In our top 10 simulations, there is large variability in modelled ice thickness in several sectors. Specifically, across the Ross Sea and

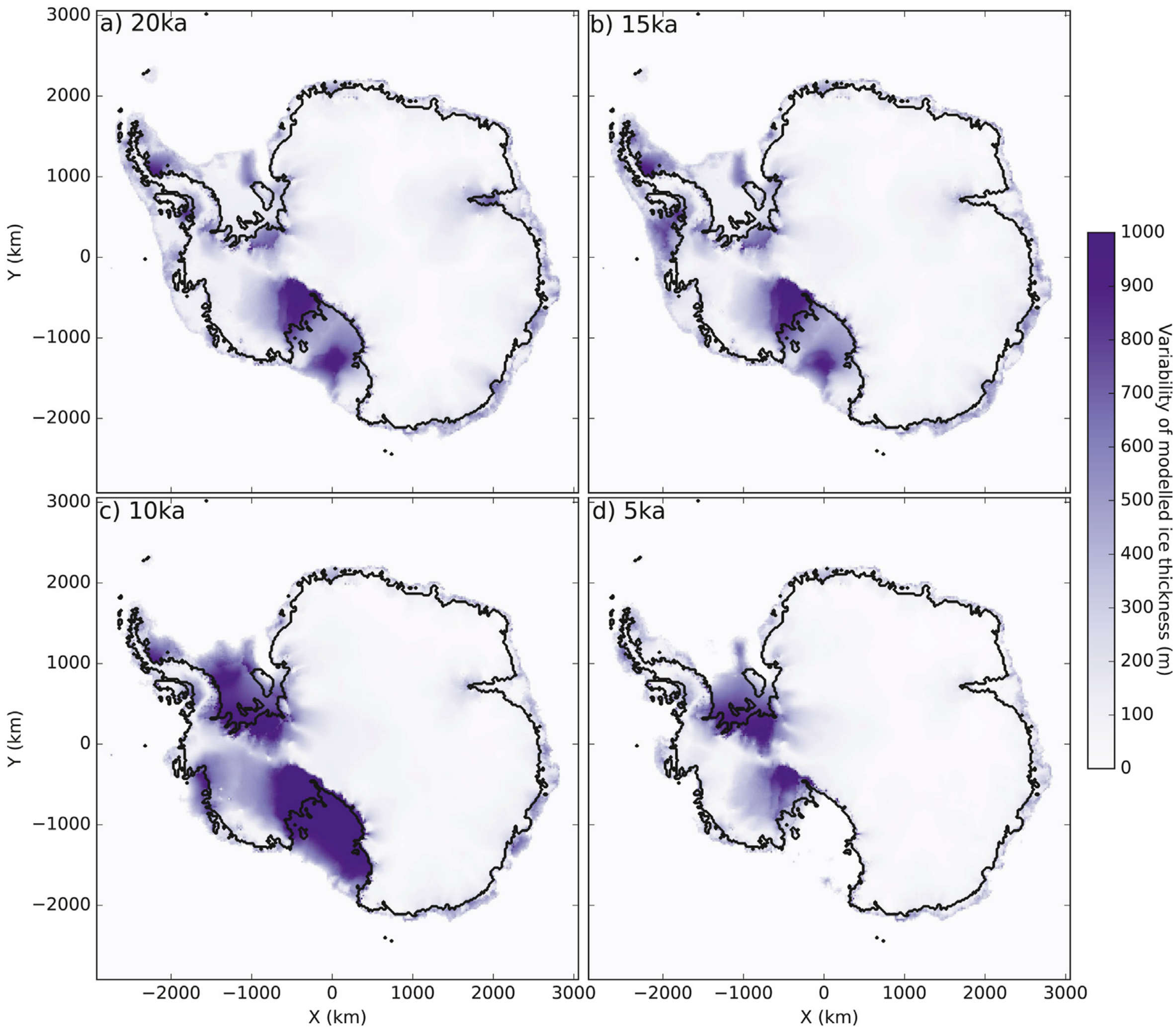

Fig. 14. Variability in modelled ice sheet thicknesses. The plots show the variation in ice thickness between the top 10 simulations, expressed as the thickness range encompassed in two standard deviations (2-sigma) relative to the mean (a) 20ka, (b)15ka, (c) 10ka and (d) 5ka. Areas of greater difference between simulations are shown by darker areas.

Weddell Sea at 20 ka, at 15 ka, and at 10 ka close to the onset of the Holocene (Fig. 14c) and across the Larsen C embayment throughout much of the deglaciation (Fig. 14a–c). As noted previously, much of the variability in ice sheet thickness at both the 20 ka and 15 ka timeslices is driven by the presence and size of embayments in the expanded ice sheet (Fig. 14a). It is notable that this variability translates to significant thickness change over a significant area of the Siple Coast (Ross), the area around the Foundation and Institute Ice Streams (Weddell), and to a lower degree in the area directly upstream from the Amery. The implication is that improved thickness constraints for 20–15 ka in these inland regions would help further discriminate between our simulations. This is in addition to the obvious point that marine geological constraints on the ice sheet extent and the embayment at 20–15 ka would also help to discriminate between simulations. Around East Antarctica there are some differences in extent across the continental shelf but with more modest thickness changes expressed inland. This may be a resolution issue as many of the ice streams feeding the short distance across the narrow continental shelf are relatively narrow compared to our grid resolution [e.g., Pittard et al., 2017]. Efforts to model the ice sheet with adaptive meshes will be important for addressing this issue [e.g., Gong et al., 2014]. The relatively minor differences around East Antarctica may also be related to the narrow continental shelf as there are relatively small variations in LGM grounded ice extent in different ensemble members (Fig. 14). Vertical differences may be driven by parameters that control vertical profile and which could be better constrained by more onshore geological observations.

For the 10 ka timeslice there are even greater areas of variability (Fig. 14c), in this case driven by the large range of grounding line positions. Some top scoring simulations having already retreated deep inland by this time (Fig. 11) with others still having grounding lines present on the outer to mid continental shelf. Marine geological records from 10 ka in the central areas of the major embayments would have significant power to discriminate between simulations but much of this area is beneath current ice shelves and thus very difficult to access even with specialist coring approaches [e.g., Smith et al., 2021].

By the 5 ka timeslice the variability in ice thickness is largely driven by the difference in Late Holocene retreat to minimum positions (Fig. 14d). Resolving between these is more challenging than for other timeslices because the differences are driven by configurations smaller than present where evidence (e.g. a cosmogenic nuclide inventory) is recorded beneath present day ice. In this case discriminating between these simulations requires drilling to bedrock to analyse cosmogenic nuclide evidence of Holocene exposure of buried nunataks (a target of several ongoing projects) or drilling beneath ice to look for Holocene marine sediments recording former grounding line retreat (Kingslake et al., 2018; Neuhaus et al., 2021). At this timeslice marine geological data has the power to discriminate between simulations with and without areas of remnant ice on the continental shelf such as between the Amundsen and Bellingshausen seas, north of Berkner Island and on both sides of the Antarctic Peninsula (Fig. 14d), but the marine data has far less power to constrain the main ice sheet. At this timeslice marine geological data has the power to discriminate between simulations with and without areas of remnant ice on the continental shelf such as between the Amundsen and Bellingshausen seas, north of Berkner Island and on both side of the Antarctic Peninsula (Fig. 14d), but the marine data has far less power to constrain the main ice sheet.

7.6. Limitations

Finally we reflect on some of the limitations of our approach, in terms of both the ensemble modelling and scoring methodology. Firstly, in order to run a large ensemble of simulations we used a relatively coarse horizontal resolution (20 km) which results in regions with complex topography being poorly represented. Such regions include the Transantarctic mountains, where ice flux from the East Antarctic Ice Sheet to the Ross Ice Shelf is underestimated along glaciers <60 km wide, and the Amery and George VI ice shelves, where flow along narrow ice shelves is poorly resolved, often leading to simulated grounding line advances in excess of geological observations. These issues contribute to the relatively poor scores achieved for the present day time-slice in our simulations; the narrow ice streams and ice shelves are unable to transport sufficient volumes of ice resulting in modelled ice that can be too thick or too advanced. Flow in areas of complex topography can also produce complicated relationships between ice and cosmogenic nuclide exposure ages from nunataks (Mas e Braga et al., 2021), an issue exacerbated by lower model resolution. It is notable that our higher scoring deglacial reconstructions tend to have higher SSAE values, reflecting the improvement in performance when flow rates are enhanced in regions that are poorly resolved at 20 km horizontal resolution. Allowing for spatially variable shallow shelf enhancement factors could also lead to better representation of ice flow in regions of complex topography. Alternatively the use of adaptive meshes in areas of complex topography could be further explored, although the computational expense may be currently prohibitive for palaeo models.

Another limitation relates to factors that exert a first order control on the position of the grounding line and the profile of the ice sheet including the conditions at the base of the ice sheet (geology, topography, presence of water), the water depth at the grounding line (linked to mantle viscosity), the temperature of the ocean, and the buttressing effect of any ice shelf or ice mélange (Pollard et al., 2018). In some cases the relationship between these factors and ice dynamics is poorly known. It is reasonable to assume that some vary spatially, especially bed conditions and mantle viscosity (Whitehouse et al., 2019), but in ways that have not been fully constrained and incorporated into models. In particular, we acknowledge that mantle viscosity varies spatially in three-dimensions, especially between East and West Antarctica. Choice of a single mantle viscosity implies trade-offs between behaviors across the continent. Furthermore, there is currently insufficient geological evidence from which to infer if there have been any past time-dependent changes to these factors that should be incorporated into models, either directly or via parameter optimisation within an ensemble modelling approach. Future efforts should focus on constraining the controls on past ice sheet change as well as documenting the actual change, for example in terms of how bed conditions evolve during deglaciation.

Any scoring approach using geological data has to deal with measurement and geological uncertainties in the constraint data, along with the limitations of representing flow through detailed topography where a large proportion of geological constraints exist (Mas e Braga et al., 2021). Our approach has been to use expert judgement and synthesis of grounding line position (Bentley et al., 2014), and to allow for a degree of temporal and spatial uncertainty (Fig. 4) in thickness and extent data, which we have termed here tolerance and error. Moreover we have developed for the first time an approach that incorporates scoring against thinning rates, which themselves incorporate and represent a range of uncertainties (Small et al., 2019). But we note that other approaches exist such as attempting to define all geological uncertainties in a Bayesian framework (Briggs et al., 2014).

Finally, we still end up with similar scores for very different ice sheet reconstructions which indicates both a need for more geological data in some key regions (Fig. 14) and that we also need to further refine our approach to identify the 'best' reconstructions. Related to this, novel approaches are required to reconstruct ice thickness change across the interior of the ice sheets where geological records are almost non-existent. Ice thickness change in the interior is likely to have been minimal away from regions of large-scale grounding line migration, but the implications for total ice volume change are significant. In particular, it is important to test the hypothesis that some regions of the ice sheet were thinner than present during the last glacial cycle, as suggested by ice core evidence [e.g., Mackintosh et al., 2014] and previous modelling studies. One promising approach is to compare or score models against internal ice architecture, such as demonstrated recently by Sutter et al. (2021). By looking at the internal layering of the ice itself, this approach has the significant advantage of fewer spatiotemporal limitations: it is possible to utilise large parts of the interior ice sheet to constrain models, not just the geological records from nunataks, marine cores, or in ice cores.

8. Conclusions

We provide a new model ensemble of Antarctic deglaciation using PISM along with a new scoring methodology for comparing model output against geological constraint data. Our approach has been to run a two-stage model ensemble of the Antarctic Ice Sheet: a first ensemble to explore a broad parameter space and a second to focus on exploring the best simulations using the higher scoring parameter combinations. Our main conclusions from this work are:

- Patterns of LGM extent in top-scoring simulations show AIS sea level contributions of 10.9–14.08 m SLE, consistent with recent published ranges.
- A wide range of retreat behaviours are exhibited in the top-scoring simulations, with differences mostly occurring in the Weddell Sea, Ross Sea and Amery-Lambert Glacier regions. Differences include LGM configurations, the timing of retreat onset, and timing of ice sheet retreat to a minimum position.
- Our top scoring simulations score more highly than four previously published models when our scoring methodology is applied.
- These best scoring simulations show early (pre-15 ka) deglaciation consistent with some marine geological data. This

modelled deglaciation is accompanied by significant reductions in volume.

- A common feature of our highest-scoring simulations is retreat of up to a few 100s of km behind the present grounding line in both the Weddell Sea and Ross Sea. This corresponds to a volume of −0.4 to −1.0 m SLE smaller than the present ice sheet. The modelled extent of the retreat is broadly consistent with a range of other work based on geological data and model studies (Bradley et al., 2015; Kingslake et al., 2018; Neuhaus et al., 2021; Venturelli et al., 2020).
- We explore four key parameters in our ensembles, and show that there are trade-offs in the best scoring simulations between three of the parameters (Shallow Ice Approximation enhancement factor, Shallow Shelf Approximation enhancement factor, lower till angle in bed strength parameterisation) that relate to ice rheology and bed strength. The fourth parameter of mantle viscosity shows a clear relationship with the retreat minima: lower viscosity tends to stabilise retreat, consistent with recent suggestions on the potential importance of grounding line stabilisation by rapid uplift (Gomez et al., 2015).
- We explore the mechanisms by which the retreat to minima, and the subsequent Late Holocene readvance occur. For re-grounding we find that both bed uplift and ice shelf thickening contribute to the re-grounding of the ice.
- Assessing the variability in our top scoring simulations allows us to provide guidance for locations where new geological constraints would have most constraining power.

Finally, one of the primary applications for these ensemble models of deglacial reconstructions tested against geological data is to use them as the ice loading components of glacial isostatic adjustment models. These GIA models are in turn used to correct satellite gravimetric measurements of contemporary ice sheet mass balance (Whitehouse, 2018). By using an ensemble approach, we suggest that the top scoring simulations could be used in GIA models and will allow propagation of a robust uncertainty estimate in the ice loading component.

9. Code and data availability

Ensemble 1, Ensemble 2 and scoring code will be available at the NERC Polar Data Centre repository.

Funding

The work was conducted as part of NERC grant NE/K003674/1 to MB and PLW. DS is supported by NERC Fellowship NE/T011963/1. We thank the Durham University facility for Advanced Research Computing (Hamilton) and the UK Archer facility for computation time. We also thank Robert Mulvaney for providing the EDML ice core record, William Roberts for the climate simulation used in climate forcing S3, and to Glenn Milne for providing the GIA Model used to create the time-varying sea level input. Development of PISM is supported by NASA grant NNX17AG65G and NSF grants PLR-1603799 and PLR-1644277. We thank two reviewers for their helpful and thorough comments which helped us clarify and improve the paper.

Author contributions

MB, PLW and MLP conceived the work. MLP led the simulations with PLW, and produced an early draft of the manuscript. DS provided the thinning rate data. All authors contributed to data interpretation and manuscript writing.

Declaration of competing interest

The authors declare that they have no known competing financial interests or personal relationships that could have appeared to influence the work reported in this paper.

Supplementary data

Supplementary data to this article can be found online at https://doi.org/10.1016/j.quascirev.2022.107800, including an explanation of DUbmap (Appendix A) and the sub-model components (Appendix B).

References

Adkins, J.F., McIntyre, K., Schrag, D.P., 2002. The salinity, temperature, and δ18o of the glacial deep ocean. Science 298, 1769–1773.

Albrecht, T., other PISM authors, 2019. PISM_PIK_1.0: PISM version as used in Albrecht, Winkelmann and Levermann,. Cryosphere. https://doi.org/10.5281/zenodo.3574033. URL: https://doi.org/10.5281/zenodo.3574033.

Albrecht, T., Winkelmann, R., Levermann, A., 2020a. Glacial-cycle simulations of the antarctic ice sheet with the parallel ice sheet model (PISM) - Part 1: boundary conditions and climatic forcing. Cryosphere 14, 599–632. https://doi.org/10.5194/tc-14-599-2020.

Albrecht, T., Winkelmann, R., Levermann, A., 2020b. Glacial-cycle simulations of the antarctic ice sheet with the parallel ice sheet model (PISM) - Part 2: parameter ensemble analysis. Cryosphere 14, 633–656. https://doi.org/10.5194/tc-14-633-2020.

Argus, D.F., Peltier, W.R., Drummond, R., Moore, A.W., 2014. The Antarctica component of postglacial rebound model ICE-6G_C (VM5a) based on GPS positioning, exposure age dating of ice thicknesses, and relative sea level histories. Geophys. J. Int. 198, 537–563. https://doi.org/10.1093/gji/ggu140.

Arndt, J.E., Larter, R.D., Hillenbrand, C.D., Sørli, S.H., Forwick, M., Smith, J.A., Wacker, L., 2020. Past ice sheet–seabed interactions in the northeastern Weddell Sea embayment, Antarctica. Cryosphere 14, 2115–2135.

Aschwanden, A., Bueler, E., Khroulev, C., Blatter, H., 2012. An enthalpy formulation for glaciers and ice sheets. J. Glaciol. 58, 441–457. https://doi.org/10.3189/2012JoG11J088.

Bentley, M.J., 1999. Volume of Antarctic ice at the Last Glacial Maximum, and its impact on global sea level change. Quat. Sci. Rev. 18, 1569–1595. https://doi.org/10.1016/S0277-3791(98)00118-8. URL: https://www.sciencedirect.com/science/article/pii/S0277379198001188.

Bentley, M.J., 2010. The Antarctic palaeo record and its role in improving predictions of future Antarctic ice sheet change. J. Quat. Sci. 25, 5–18. URL: https://onlinelibrary.wiley.com/doi/abs/10.1002/jqs.1287, doi:https://doi.org/10.1002/jqs.1287, arXiv:https://onlinelibrary.wiley.com/doi/pdf/10.1002/jqs.1287.

Bentley, M.J., Ó Cofaigh, C., Anderson, J.B., Conway, H., Davies, B., Graham, A.G.C., Hillenbrand, C.D., Hodgson, D.A., Jamieson, S.S.R., Larter, R.D., Mackintosh, A., Smith, J.A., Verleyen, E., Ackert, R.P., Bart, P.J., Berg, S., Brunstein, D., Canals, M., Colhoun, E.A., Crosta, X., Dickens, W.A., Domack, E., Dowdeswell, J.A., Dunbar, R., Ehrmann, W., Evans, J., Favier, V., Fink, D., Fogwill, C.J., Glasser, N.F., Gohl, K., Golledge, N.R., Goodwin, I., Gore, D.B., Greenwood, S.L., Hall, B.L., Hall, K., Hedding, D.W., Hein, A.S., Hocking, E.P., Jakobsson, M., Johnson, J.S., Jomelli, V., Jones, R.S., Klages, J.P., Kristoffersen, Y., Kuhn, G., Leventer, A., Licht, K., Lilly, K., Lindow, J., Livingstone, S.J., Massé, G., McGlone, M.S., McKay, R.M., Melles, M., Miura, H., Mulvaney, R., Nel, W., Nitsche, F.O., O'Brien, P.E., Post, A.L., Roberts, S.J., Saunders, K.M., Selkirk, P.M., Simms, A.R., Spiegel, C., Stolldorf, T.D., Sugden, D.E., van der Putten, N., van Ommen, T., Verfaillie, D., Vyverman, W., Wagner, B., White, D.A., Witus, A.E., Zwartz, D., 2014. A community-based geological reconstruction of Antarctic Ice Sheet deglaciation since the Last Glacial Maximum. Quat. Sci. Rev. 100, 1–9. https://doi.org/10.1016/j.quascirev.2014.06.025.

Bentley, M.J., Hein, A., Sugden, D., Whitehouse, P.L., Shanks, R., Xu, S., Freeman, S., 2017. Deglacial history of the Pensacola Mountains, Antarctica from glacial geomorphology and cosmogenic nuclide surface exposure dating. Quat. Sci. Rev. 158, 58–76.

Bintanja, R., van de Wal, R.S.W., 2008. North American ice-sheet dynamics and the onset of 100,000-year glacial cycles. Nature 454, 869–872. https://doi.org/10.1038/nature07158.

Braconnot, P., Harrison, S.P., Otto-Bliesner, B., Abe-Ouchi, A., Jungclaus, J., Peterschmitt, J.Y., 2011. The Paleoclimate Modeling Intercomparison Project contribution to CMIP5. CLIVAR Exchanges 56.

Bradley, S., Siddall, M., Milne, G., Masson-Delmotte, V., Wolff, E., 2013. Combining ice core records and ice sheet models to explore the evolution of the East Antarctic Ice Sheet during the last interglacial period. Global Planet. Change 100, 278–290.

Bradley, S.L., Hindmarsh, R.C., Whitehouse, P.L., Bentley, M.J., King, M.A., 2015. Low post-glacial rebound rates in the Weddell Sea due to Late Holocene ice-sheet readvance. Earth Planet Sci. Lett. 413, 79–89.

Briggs and Tarasov, 2013. How to evaluate model-derived deglaciation

chronologies: a case study using Antarctica. Quat. Sci. Rev. 63, 109–127. https://doi.org/10.1016/j.quascirev.2012.11.021".
Briggs, R.D., Pollard, D., Tarasov, L., 2014. A data-constrained large ensemble analysis of Antarctic evolution since the Eemian. Quat. Sci. Rev. 103, 91–115. https://doi.org/10.1016/j.quascirev.2014.09.003.
Bueler, E., Brown, J., Lingle, C., 2007. Exact solutions to the thermomechanically coupled shallow-ice approximation: effective tools for verification. J. Glaciol. 53, 499–516. https://doi.org/10.3189/002214307783258396.
Clark, P.U., Mix, A.C., 2002. Ice sheets and sea level of the Last Glacial Maximum. Quat. Sci. Rev. 21, 1–7. https://doi.org/10.1016/S0277-3791(01)00118-4.
Cuffey, K.M., Paterson, W.S.B., 2010. The Physics of Glaciers. Academic Press.
DeConto, R.M., Pollard, D., 2016. Contribution of Antarctica to past and future sea-level rise. Nature 531, 591–597. https://doi.org/10.1038/nature17145.
Edwards, T.L., Brandon, M.A., Durand, G., Edwards, N.R., Golledge, N.R., Holden, P.B., Nias, I.J., Payne, A.J., Ritz, C., Wernecke, A., 2019. Revisiting Antarctic ice loss due to marine ice-cliff instability 566, 58–64. https://doi.org/10.1038/s41586-019-0901-4.
Ely, J.C., Clark, C.D., Small, D., Hindmarsh, R.C.A., 2019. Atat 1.1, the automated timing accordance tool for comparing ice-sheet model output with geochronological data. Geosci. Model Dev. (GMD) 12, 933–953. https://doi.org/10.5194/gmd-12-933-2019. https://gmd.copernicus.org/articles/12/933/2019/.
Fretwell, P., Pritchard, H.D., Vaughan, D.G., Bamber, J.L., Barrand, N.E., Bell, R., Bianchi, C., Bingham, R.G., Blankenship, D.D., Casassa, G., Catania, G., Callens, D., Conway, H., Cook, A.J., Corr, H.F.J., Damaske, D., Damm, V., Ferraccioli, F., Forsberg, R., Fujita, S., Gim, Y., Gogineni, P., Griggs, J.A., Hindmarsh, R.C.A., Holmlund, P., Holt, J.W., Jacobel, R.W., Jenkins, A., Jokat, W., Jordan, T., King, E.C., Kohler, J., Krabill, W., Riger-Kusk, M., Langley, K.A., Leitchenkov, G., Leuschen, C., Luyendyk, B.P., Matsuoka, K., Mouginot, J., Nitsche, F.O., Nogi, Y., Nost, O.A., Popov, S.V., Rignot, E., Rippin, D.M., Rivera, A., Roberts, J., Ross, N., Siegert, M.J., Smith, A.M., Steinhage, D., Studinger, M., Sun, B., Tinto, B.K., Welch, B.C., Wilson, D., Young, D.A., Xiangbin, C., Zirizzotti, A., 2013. Bedmap2: improved ice bed, surface and thickness datasets for Antarctica. Cryosphere 7, 375–393. https://doi.org/10.5194/tc-7-375-2013.
Frieler, K., Clark, P.U., He, F., Buizert, C., Reese, R., Ligtenberg, S.R., Van Den Broeke, M.R., Winkelmann, R., Levermann, A., 2015. Consistent evidence of increasing Antarctic accumulation with warming. Nat. Clim. Change 5, 348–352.
Galton-Fenzi, B.K., Maraldi, C., Coleman, R., Hunter, J., 2008. The cavity under the Amery Ice Shelf, East Antarctica. J. Glaciol. 54, 881–887. https://doi.org/10.3189/002214308787779898.
Golledge, N.R., Fogwill, C.J., Mackintosh, A.N., Buckley, K.M., 2012. Dynamics of the Last Glacial Maximum Antarctic ice-sheet and its response to ocean forcing. Proc. Natl. Acad. Sci. USA 109, 16052–16056. https://doi.org/10.1073/pnas.1205385109.
Golledge, N.R., Menviel, L., Carter, L., Fogwill, C.J., England, M.H., Cortese, G., Levy, R.H., 2014. Antarctic contribution to Meltwater Pulse 1a from reduced Southern Ocean overturning. Nat. Commun. 5, 1–10.
Golledge, N.R., Kowalewski, D.E., Naish, T.R., Levy, R.H., Fogwill, C.J., Gasson, E.G.W., 2015. The multi-millennial Antarctic commitment to future sea-level rise. Nature 526, 421–425. https://doi.org/10.1038/nature15706.
Gomez, N., Pollard, D., Mitrovica, J.X., 2013. A 3-D coupled ice sheet - sea level model applied to Antarctica through the last 40 ky. Earth Planet Sci. Lett. 384, 88–99. https://doi.org/10.1016/j.epsl.2013.09.042.
Gomez, N., Pollard, D., Holland, D., 2015. Sea-level feedback lowers projections of future Antarctic ice-sheet mass loss. Nat. Commun. 6, 1–8.
Gong, Y., Cornford, S., Payne, A., 2014. Modelling the response of the Lambert Glacier–Amery ice shelf system, East Antarctica, to uncertain climate forcing over the 21st and 22nd centuries. Cryosphere 8, 1057–1068.
Gowan, E.J., Zhang, X., Khosravi, S., Rovere, A., Stocchi, P., Hughes, A.L., Gyllencreutz, R., Mangerud, J., Svendsen, J.I., Lohmann, G., 2021. A new global ice sheet reconstruction for the past 80 000 years. Nat. Commun. 12, 1–9.
Greenbaum, J.S., Blankenship, D.D., Young, D.A., Richter, T.G., Roberts, J.L., Aitken, A.R.A., Legresy, B., Schroeder, D.M., Warner, R.C., van Ommen, T.D., Siegert, M.J., 2015. Ocean access to a cavity beneath Totten Glacier in East Antarctica. Nat. Geosci. 8, 294–298. https://doi.org/10.1038/ngeo2388.
Greenwood, S.L., Simkins, L.M., Halberstadt, A.R.W., Prothro, L.O., Anderson, J.B., 2018. Holocene reconfiguration and readvance of the East Antarctic Ice Sheet. Nat. Commun. 9, 1–12.
Halberstadt, A.R.W., Simkins, L.M., Greenwood, S.L., Anderson, J.B., 2016. Past ice-sheet behaviour: retreat scenarios and changing controls in the Ross Sea, Antarctica. Cryosphere 10, 1003–1020.
Hein, A.S., Marrero, S.M., Woodward, J., Dunning, S.A., Winter, K., Westoby, M.J., Freeman, S.P., Shanks, R.P., Sugden, D.E., 2016. Mid-holocene pulse of thinning in the Weddell Sea sector of the West Antarctic Ice Sheet. Nat. Commun. 7, 1–8.
Hillenbrand, C.D., Bentley, M.J., Stolldorf, T.D., Hein, A.S., Kuhn, G., Graham, A.G., Fogwill, C.J., Kristoffersen, Y., Smith, J.A., Anderson, J.B., et al., 2014. Reconstruction of changes in the Weddell Sea sector of the Antarctic Ice Sheet since the Last Glacial Maximum. Quat. Sci. Rev. 100, 111–136.
Hodgson, D.A., Jordan, T.A., Rydt, J.D., Fretwell, P.T., Seddon, S.A., Becker, D., Hogan, K.A., Smith, A.M., Vaughan, D.G., 2019. Past and future dynamics of the Brunt Ice Shelf from seabed bathymetry and ice shelf geometry. Cryosphere 13, 545–556.
Ivins, E.R., James, T.S., 2005. Antarctic glacial isostatic adjustment: a new assessment. Antarct. Sci. 17, 541. https://doi.org/10.1017/S0954102005002968.
Ivins, E.R., James, T.S., Wahr, J., Schrama, E.J.O., Landerer, F.W., Simon, K.M., 2013. Antarctic contribution to sea level rise observed by GRACE with improved GIA correction. J. Geophys. Res. 118, 3126–3141. https://doi.org/10.1002/jgrb.50208.
Johnson, J.S., Bentley, M.J., Smith, J.A., Finkel, R., Rood, D., Gohl, K., Balco, G., Larter, R.D., Schaefer, J., 2014. Rapid thinning of Pine Island Glacier in the Early Holocene. Science 343, 999–1001.
Jones, R., Mackintosh, A.N., Norton, K.P., Golledge, N.R., Fogwill, C.J., Kubik, P.W., Christl, M., Greenwood, S.L., 2015. Rapid Holocene thinning of an East Antarctic outlet glacier driven by marine ice sheet instability. Nat. Commun. 6, 1–9.
Kachuck, S.B., Martin, D.F., Bassis, J.N., Price, S.F., 2020. Rapid viscoelastic deformation slows marine ice sheet instability at Pine Island Glacier. Geophys. Res. Lett. 47 e2019GL086446.
Kingslake, J., Scherer, R.P., Albrecht, T., Coenen, J., Powell, R.D., Reese, R., Stansell, N.D., Tulaczyk, S., Wearing, M.G., Whitehouse, P.L., 2018. Extensive retreat and re-advance of the West Antarctic Ice Sheet during the Holocene 558, 430–434. https://doi.org/10.1038/s41586-018-0208-x.
Lambeck, K., Rouby, H., Purcell, A., Sun, Y., Sambridge, M., 2014. sea level and global ice volumes from the Last Glacial Maximum to the Holocene. Proc. Natl. Acad. Sci. USA 111, 15296–15303. https://doi.org/10.1073/pnas.1411762111.
Larter, R.D., Anderson, J.B., Graham, A.G., Gohl, K., Hillenbrand, C.D., Jakobsson, M., Johnson, J.S., Kuhn, G., Nitsche, F.O., Smith, J.A., et al., 2014. Reconstruction of changes in the Amundsen Sea and Bellingshausen Sea sector of the West Antarctic Ice Sheet since the Last Glacial Maximum. Quat. Sci. Rev. 100, 55–86.
Levermann, A., Albrecht, T., Winkelmann, R., Martin, M.A., Haseloff, M., Joughin, I., 2012. Kinematic first-order calving law implies potential for abrupt ice-shelf retreat. Cryosphere 6, 273–286. https://doi.org/10.5194/tc-6-273-2012. https://www.the-cryosphere.net/6/273/2012/.
Lingle, C.S., Clark, J.A., 1985. A numerical model of interactions between a marine ice sheet and the solid earth: application to a West Antarctic ice stream. Journal of Geophysical Research: Oceans 90, 1100–1114.
Livingstone, S.J., , Cofaigh, C.Ó., Stokes, C.R., Hillenbrand, C.D., Vieli, A., Jamieson, S.S., 2012. Antarctic palaeo-ice streams. Earth Sci. Rev. 111, 90–128.
Lowry, D.P., Golledge, N.R., Bertler, N.A., Jones, R.S., McKay, R., 2019. Deglacial grounding-line retreat in the Ross Embayment, Antarctica, controlled by ocean and atmosphere forcing. Sci. Adv. 5 eaav8754.
Mackintosh, A., Golledge, N., Domack, E., Dunbar, R., Leventer, A., White, D., Pollard, D., DeConto, R., Fink, D., Zwartz, D., et al., 2011. Retreat of the East Antarctic Ice Sheet during the last glacial termination. Nat. Geosci. 4, 195–202.
Mackintosh, A.N., Verleyen, E., O'Brien, P.E., White, D.A., Jones, R.S., McKay, R., Dunbar, R., Gore, D.B., Fink, D., Post, A.L., et al., 2014. Retreat history of the East Antarctic Ice Sheet since the Last Glacial Maximum. Quat. Sci. Rev. 100, 10–30.
Maris, M.N.A., de Boer, B., Ligtenberg, S.R.M., Crucifix, M., van de Berg, W.J., Oerlemans, J., 2014. Modelling the evolution of the Antarctic Ice Sheet since the last interglacial. Cryosphere 8, 1347–1360. https://doi.org/10.5194/tc-8-1347-2014.
Martin, M., Winkelmann, R., Haseloff, M., Albrecht, T., Bueler, E., Khroulev, C., Levermann, A., 2011. The Potsdam Parallel Ice Sheet Model (PISM-PIK)–part 2: dynamic equilibrium simulation of the Antarctic Ice Sheet. Cryosphere 5, 727–740.
Martinerie, P., Lipenkov, V.Y., Raynaud, D., Chappellaz, J., Barkov, N., Lorius, C., 1994. Air content paleo record in the Vostok ice core (Antarctica): a mixed record of climatic and glaciological parameters. Journal of Geophysical Research: Atmospheres 99, 10565–10576.
Martos, Y.M., Catalán, M., Jordan, T.A., Golynsky, A., Golynsky, D., Eagles, G., Vaughan, D.G., 2017. Heat flux distribution of Antarctica unveiled. Geophys. Res. Lett. 44, 11,417–11,426. https://doi.org/10.1002/2017GL075609. URL: https://agupubs.onlinelibrary.wiley.com/doi/abs/10.1002/2017GL075609.
Mas e Braga, M., Selwyn Jones, R., Newall, J.C.H., Rogozhina, I., Andersen, J.L., Lifton, N.A., Stroeven, A.P., 2021. Nunataks as barriers to ice flow: implications for palaeo ice sheet reconstructions. The Cryosphere 15, 4929–4947. https://doi.org/10.5194/tc-15-4929-2021.
Matsuoka, K., Hindmarsh, R.C., Moholdt, G., Bentley, M.J., Pritchard, H.D., Brown, J., Conway, H., Drews, R., Durand, G., Goldberg, D., et al., 2015. Antarctic ice rises and rumples: their properties and significance for ice-sheet dynamics and evolution. Earth Sci. Rev. 150, 724–745.
Milne, G.A., Mitrovica, J.X., 1996. Postglacial sea-level change on a rotating Earth: first results from a gravitationally self-consistent sea-level equation. Geophys. J. Int. 126, F13–F20. https://doi.org/10.1111/j.1365-246X.1996.tb04691.x.
Napoleoni, F., Jamieson, S.S., Ross, N., Bentley, M.J., Rivera, A., Smith, A.M., Siegert, M.J., Paxman, G.J., Gacitúa, G., Uribe, J.A., et al., 2020. Subglacial lakes and hydrology across the Ellsworth Subglacial Highlands, West Antarctica. Cryosphere 14, 4507–4524.
Neuhaus, S.U., Tulaczyk, S.M., Stansell, N.D., Coenen, J.J., Scherer, R.P., Mikucki, J.A., Powell, R.D., 2021. Did Holocene climate changes drive West Antarctic grounding line retreat and readvance? Cryosphere 15, 4655–4673. https://doi.org/10.5194/tc-15-4655-2021. URL: https://tc.copernicus.org/articles/15/4655/2021/.
Paxman, G.J.G, Jamieson, S.S.R., Fausto, F., Bentley, M.J., Ross, N., Armadillo, E., Gasson, E.G.W., Leitchenkov, G., DeConto, R.M., 2018. Bedrock erosion surfaces record former East Antarctic Ice Sheet extent. Geophys. Res. Lett. 45. https://doi.org/10.1029/2018GL077268.
Peltier, W.R., 2004. Global glacial isostasy and the surface of the ice-age earth: the ICE-5G (VM2) model and GRACE. Annu. Rev. Earth Planet Sci. 32, 111–149. https://doi.org/10.1146/annurev.earth.32.082503.144359.
Phipps, S.J., Roberts, J.L., King, M.A., 2021. An iterative process for efficient optimisation of parameters in geoscientific models: a demonstration using the Parallel

Ice Sheet Model (PISM) version 0.7. 3. Geosci. Model Dev. (GMD) 14, 5107–5124.
Pittard, M.L., 2016. Ph.D. thesis. In: The Dynamics of the Lambert-Amery Glacial System and its Response to Climatic Variations. University of Tasmania.
Pittard, M., Galton-Fenzi, B., Watson, C., Roberts, J., 2017. Future sea level change from Antarctica's Lambert-Amery glacial system. Geophys. Res. Lett. 44, 7347–7355.
Pollard, D., DeConto, R.M., Alley, R.B., 2018. A continuum model (psumel1) of ice mélange and its role during retreat of the Antarctic Ice Sheet. Geosci. Model Dev. (GMD) 11, 5149–5172.
Reese, R., Albrecht, T., Mengel, M., Asay-Davis, X., Winkelmann, R., 2018. Antarctic sub-shelf melt rates via PICO. Cryosphere 12, 1969–1985. https://doi.org/10.5194/tc-12-1969-2018.
Sasgen, I., Martín-Español, A., Horvath, A., Klemann, V., Petrie, E.J., Wouters, B., Horwath, M., Pail, R., Bamber, J.L., Clarke, P.J., Konrad, H., Drinkwater, M.R., 2017. Joint inversion estimate of regional glacial isostatic adjustment in Antarctica considering a lateral varying Earth structure (ESA STSE Project REGINA). Geophys. J. Int. 211, 1534–1553. https://doi.org/10.1093/gji/ggx368.
Schmidtko, S., Heywood, K.J., Thompson, A.F., Aoki, S., 2014. Multidecadal warming of Antarctic waters. Science 346, 1227–1231. https://doi.org/10.1126/science.1256117.
Seroussi, H., Nowicki, S., Simon, E., Abe-Ouchi, A., Albrecht, T., Brondex, J., Cornford, S., Dumas, C., Gillet-Chaulet, F., Goelzer, H., et al., 2019. INITMIP-Antarctica: an ice sheet model initialization experiment of ISMIP6. Cryosphere 13, 1441–1471.
Shepherd, A., Ivins, E.R., Barletta, A.G., Bentley, V.R., Bettadpur, M.J., Briggs, S., Bromwich, K.H., Forsberg, D.H., Galin, R., Horwath, N., Jacobs, M., Joughin, S., King, I., Lenaerts, M.A., Li, J.T.M., Ligtenberg, J., Luckman, S.R.M., Luthcke, A., McMillan, S.B., Meister, M., Milne, R., Mouginot, G., Muir, J., Nicolas, A., Paden, J.P., Payne, J., Pritchard, A.J., Rignot, H., Rott, E., Sørensen, H., Scambos, L.S., Scheuchl, T.A., Schrama, B., Smith, E.J.O., Sundal, B., van Angelen, A.V., van de Berg, J.H., van den Broeke, W.J., Vaughan, M.R., Velicogna, D.G., Wahr, I., Whitehouse, J., Wingham, P.L., Yi, D.J., Young, D., , D., Zwally, H.J., 2012. A reconciled estimate of ice-sheet mass balance. Science 338, 1183. https://doi.org/10.1126/science.1228102.
Siegert, M.J., Kingslake, J., Ross, N., Whitehouse, P.L., Woodward, J., Jamieson, S.S., Bentley, M.J., Winter, K., Wearing, M., Hein, A.S., et al., 2019. Major ice sheet change in the Weddell Sea sector of West Antarctica over the last 5,000 years. Rev. Geophys. 57, 1197–1223.
Simms, A.R., Lisiecki, L., Gebbie, G., Whitehouse, P.L., Clark, J.F., 2019. Balancing the Last Glacial Maximum (LGM) sea-level budget. Quat. Sci. Rev. 205, 143–153. https://doi.org/10.1016/j.quascirev.2018.12.018.
Small, D., Bentley, M.J., Jones, R.S., Pittard, M.L., Whitehouse, P.L., 2019. Antarctic ice sheet palaeo-thinning rates from vertical transects of cosmogenic exposure ages. Quat. Sci. Rev. 206, 65–80. https://doi.org/10.1016/j.quascirev.2018.12.024.
Smith, J., Hillenbrand, C.D., Subt, C., Rosenheim, B., Frederichs, T., Ehrmann, W., Andersen, T., Wacker, L., Makinson, K., Anker, P., et al., 2021. History of the Larsen C ice shelf reconstructed from sub–ice shelf and offshore sediments. Geology 49 (8), 978–982. https://doi.org/10.1130/G48503.1.
Spector, P., Stone, J., Cowdery, S.G., Hall, B., Conway, H., Bromley, G., 2017. Rapid Early-Holocene deglaciation in the Ross Sea, Antarctica. Geophys. Res. Lett. 44, 7817–7825.
Stone, J.O., Balco, G.A., Sugden, D.E., Caffee, M.W., Sass, L.C., Cowdery, S.G., Siddoway, C., 2003. Holocene deglaciation of Marie Byrd Land, West Antarctica. Science 299, 99–102.
Sutter, J., Fischer, H., Eisen, O., 2021. Investigating the internal structure of the Antarctic Ice Sheet: the utility of isochrones for spatiotemporal ice-sheet model calibration. Cryosphere 15, 3839–3860.
Van den Berg, J., Van de Wal, R., Milne, G., Oerlemans, J., 2008. Effect of isostasy on dynamical ice sheet modeling: a case study for Eurasia. J. Geophys. Res. Solid Earth 113.
van Wessem, J.M., Reijmer, C.H., Morlighem, M., Mouginot, J., Rignot, E., Medley, B., Joughin, I., Wouters, B., Depoorter, M.A., Bamber, J.L., Lenaerts, J.T.M., van de Berg, W.J., van den Broeke, M.R., van Meijgaard, E., 2014. Improved representation of East Antarctic surface mass balance in a regional atmospheric climate model. J. Glaciol. 60, 761–770. https://doi.org/10.3189/2014JoG14J051.
Venturelli, R., Siegfried, M., Roush, K., Li, W., Burnett, J., Zook, R., Fricker, H., Priscu, J., Leventer, A., Rosenheim, B., 2020. Mid-Holocene grounding line retreat and readvance at Whillans Ice Stream, West Antarctica. Geophys. Res. Lett. 47 e2020GL088476.
Watanabe, O., Kamiyama, K., Motoyama, H., Fujii, Y., Shoji, H., Satow, K., 1999. The palaeoclimate record in the ice core from Dome Fuji station, Antarctica. Ann. Glaciol. 29, 176–178. https://doi.org/10.3189/172756499781821553.
Werner, M., Jouzel, J., Masson-Delmotte, V., Lohmann, G., 2018. Reconciling glacial Antarctic water stable isotopes with ice sheet topography and the isotopic paleothermometer. Nat. Commun. 9, 1–10.
Whitehouse, P.L., 2018. Glacial isostatic adjustment modelling: historical perspectives, recent advances, and future directions. Earth Surf. Dyn. 6, 401–429. https://doi.org/10.5194/esurf-6-401-2018.
Whitehouse, P.L., Bentley, M.J., Le Brocq, A.M., 2012a. A deglacial model for Antarctica: geological constraints and glaciological modelling as a basis for a new model of Antarctic glacial isostatic adjustment. Quat. Sci. Rev. 32, 1–24. https://doi.org/10.1016/j.quascirev.2011.11.016.
Whitehouse, P.L., Bentley, M.J., Milne, G.A., King, M.A., Thomas, I.D., 2012b. A new glacial isostatic adjustment model for Antarctica: calibrated and tested using observations of relative sea-level change and present-day uplift rates. Geophys. J. Int. 190, 1464–1482. https://doi.org/10.1111/j.1365-246X.2012.05557.x.
Whitehouse, P.L., Bentley, M.J., Vieli, A., Jamieson, S.S., Hein, A.S., Sugden, D.E., 2017. Controls on Last Glacial Maximum ice extent in the Weddell Sea Embayment, Antarctica. J. Geophys. Res.: Earth Surf. 122, 371–397.
Whitehouse, P.L., Gomez, N., King, M.A., Wiens, D.A., 2019. Solid earth change and the evolution of the Antarctic Ice Sheet. Nat. Commun. 10, 503. https://doi.org/10.1038/s41467-018-08068-y.
Winkelmann, R., Martin, M.A., Haseloff, M., Albrecht, T., Bueler, E., Khroulev, C., Levermann, A., 2011. The Potsdam Parallel Ice Sheet Model (PISM-PIK) - Part 1: model description. Cryosphere 5, 715–726. https://doi.org/10.5194/tc-5-715-2011.
Zwally, H.J., Giovinetto, M.B., Beckley, M.A., Saba, J.L., 2012. Antarctic and Greenland drainage systems, gsfc cryospheric sciences laboratory. Available at icesat4. gsfc. nasa. gov/cryo_data/ant_grn_drainage_systems. php. (Accessed 1 March 2015).